BIMA memo series 17

Design and Measurements of the Conical Corrugated Feed Horns for the BIMA Array

Xiaolei Zhang

Radio Astronomy Laboratory and Dept. of EECS

University of California, Berkeley

September. 9, 1991

Abstract

A new conical corrugated feed horn was designed and fabricated in the fall of 1990 as a test model for the upgrading BIMA antennas. The fractional single-mode operation range of this feed horn is near 50%. The improved design of the mode-launching region allows much superior performances to be achieved on the new feed horn compared to the existing feed horns on the Hat Creek antennas, in terms of impedance matching, beam symmetry and crosspolarization characteristics, as well as effective matching to the telescope focal region fields in order to obtain higher aperture and beam efficiencies. Over most of the operation range of 70 - 115 GHz, the return loss level is reduced from the old value of around - 17dB to around - 30dB, crosspolarization level reduced from around - 20dB to around - 35dB. Using a phase corrector dielectric lens in front of the conical horn aperture, the theoretical aperture efficiency of this new optical system (including illumination efficiency and spillover efficiency) is around 78 - 82 % over a 30 % bandwidth, compared to the value of 72 - 74 % for the existing optical design. Introducing a tertiary lens further improves the theoretical aperture efficiency to about 84%.

The drastic fall-off of the aperture efficiency at the high frequency end of the band on all three of the present Hat Creek antennas (measured value of 25 - 50% instead of the theoretical ~ 70%), can not be fully accounted for by the surface loss and feed-leg scatterings. Possible reasons for the dropoff of the aperture efficiency on the existing system is also analysed here from the point of view of the old feed horn performances. Measurements on the characteristics of the old Hat Creek horns, holographical measurements of the dish illumination patterns, compared with the calculation results, seem to support the arguments.

I. Quest for a High Performance Corrugated Feed Horn

The corrugated feed horns currently used on the antennas of the Hat Creek millimeter interferometer follow a design (Fig.1) originally developed at the Jet Propulsion Laboratory and the Lawrance Berkeley Laboratory for doing cosmic microwave background measurements[1]. To meet their specific requirements, the result of this design is one which has relatively low sidelobes on the copolar radiation patterns, whereas its operation bandwidth is very narrow, and its crosspolarization and return-loss characteristics poor. What more, at the high frequency end of the operation band, the invasion of EH type higher order modes caused the beam patterns to be severely distorted, a significant amount of the power to be radiated in the crosspolarised component, and phase losses due to the E and H plane phase unsymmetry are also increased. This is responsible, at least in part, for the severe aperture efficiency drop near the high frequency end of the operation band on the current Hat Creek antennas. This is particularly worrisome for the existing system, since at the higher frequency end (115 GHz) lies the carbon monoxide $J = 1 \rightarrow 0$ rotational transition line, which is an extremely important line for astrophysical studies, and atmospheric extinction at 115 GHz already cause the line to be extremely weak. In the recent expansion and upgrading of the BIMA array, an improved design of the feed horn is therefore needed, in order to reduce its contributions to the system loss and noise, and to achieve better matching to the telescope focal region fields.

The idea and prototypes of the corrugated feed horns were originated in the early 1960's to achieve low sidelobe and symmetric beam radiation patterns. Diffraction analysis has shown that most of the backlobe structure of a pyramidal horn results from energy diffracted by the E-plane edges. This can be understood by the well known fact that the far field pattern of a horn antenna is the Fourier transform of its aperture field distribution. The discontinuity of the step distribution at the E plane edge of a pyramidal horn is responsible for the higher sidelobe levels in its farfield. The E- and H-plane radiation patterns of the pyramidal horns are also non-symmetric.

On the other hand, the single (dominant) mode corrugated feed horn has mainly a $J_0(\kappa r)\hat{x}$ distribution over the aperture, with the first zero of J_0 falling on the edge of the aperture. This distribution has a much smoother truncation near the edge of the aperture and thus a much lower sidelobe level in the far field patterns. It also offers a nearly perfect circularly symmetric and linearly polarized beam. By doing mode synthesis using many HE type of feed horn modes, an even smoother aperture distribution and even lower sidelobe levels in the far field can be achieved.

Although a complete understanding of the feed horn working principles involves the solution of Maxwell's equations under the boundary condition of the feed horn corrugations, the process of which I will describe in detail in the later sections, the main result of this solution is easy to understand. A small flare-angled corrugated feed horn can be approximated by a corrugated waveguide of constant cross-section, with the effect of the horn flare angle being taken into account by superposing a spherical cap phase distribution to the aperture field solution. In corrugated waveguide of large

enough diameter, two sets of modes can propagate. These are termed HE_{1n} and EH_{1n} modes. (n is the number of the roots of either the first order Bessel function J_1, or the number of roots of J_1's first derivative. These roots appear in the expressions of the HE_{11} and EH_{11} fields, respectively). Here EH_{1n} modes are highly undesirable, since they cause beam asymmetry and crosspolarized radiation, which not only contaminates the polarization purity, but also lowers the aperture efficiency of the telescope system. The HE_{1n} modes, on the other hand, can all be used, at least in principle, to do pattern synthesis. In practice this is not always so easy and to our advantage: first, an analytical approach is not available to control the amplitude of each mode entering the horn. The conventional practice is to employ a numerical program [2] which models the horn through cascading the scattering matrices of each cylindrical section, changing the design parameters for the mode-launching region each time, and to obtain the desired radiation patterns through trial and error. The bandwidth of the resulting design is often not optimized and can get as narrow as 5% to 10%. Secondly, as detailed analysis shows, in the mode launching region the EH type higher order modes and the HE type higher order modes have very similar cutoff frequencies. That is to say, it is very hard to excite only the HE type higher order modes to do the pattern synthesis, without at the same time coupling in the EH set of modes.

Due to the above mentioned complications involved in designing a multi-mode horn, we decided to make our first test model a single-mode horn, to achieve the widest possible bandwidth and to investigate the ways to improve the feed horn performance on several important merits. Single mode horns generally have a sidelobe level of about - 25 dB, which is good enough for our current applications.

In the design of the corrugated feed horns, the so called "throat" or mode- launching region is the most important and most difficult part. Since when the horn starts to flare to bigger aperture, the size of the horn will allow almost all the HE_{1n} and EH_{1n} modes to propagate, we can only select the modes in the throat region, where the horn dimension is still small enough to allow the cutoff of the unwanted modes. Besides acting as the mode launcher and selector, the throat region should also be an impedance transformer, achieving the smooth conversion of the circular waveguide TE_{11} mode to the corrugated waveguide HE_{11} mode. The impedance matching and mode selecting function should work over the entire bandwidth we are interested in. The throat region on the old horn (Fig.1) consisted of only one deep groove, and has very poor impedance matching and bandwidth properties. In the new design of the feed horn (Fig.2), carefully chosen parameters for the throat region allow almost all of the above mentioned goals to be achieved. It has a single-mode operation range of about 48% (the widest possible), and the return loss over most of the bandwidth is around or below - 30 dB. In the design process, a new understanding of the ways to simultaneously achieve wideband single-mode operation and wideband impedance matching has also been obtained, which so far has not been reported in the literature.

The design for the main body of the feed horn concerns flaring the horn to the correct aperture size with a proper flare angle, in order to satisfy the requirement placed by the telescope optics. This amounts to seeking the best overlap between the

telescope focal region fields and the field horn aperture fields. With the optics design on the existing system, the theoretical aperture efficiency is about 72-74% (this is without taking into account of the cross-polarization loss and phase loss caused by higher order modes, and also without considering feed-leg scattering and surface-roughness loss). This number can be increased to about 78-82% if we realize that part of the loss in aperture efficiency is due to the amplitude- and phase-mismatch loss. To be more specific, if we place the Cassegrain focus inside a feed horn of moderate size, change its positions to search for the best aperture efficiency match, we found that the wavefront curvature and the amplitude distribution of the telescope field near the horn aperture usually does not match exactly with those on the feed horn aperture. Thus when we overlap the two fields to calculate aperture efficiency we lose some amount due to this mismatch. This loss is the equivalence of the illumination and spillover loss if we do the overlap of the fields on the telescope dish surface to calculate aperture efficiency.

A better amplitude and phase match can be achieved by placing the Cassegrain focus right at the position of the horn aperture, so that the telescope field now has a flat wavefront, and to produce a flat wavefront also at the aperture of the match-sized feed horn. To do this, we could either use a dielectric lens on the horn aperture to act as a phase corrector, or gradually shape the body of the horn so that at the aperture it becomes a section of the corrugated waveguide again. This later design has been proposed and analysed by a group of researchers [3,4]. Since it involves fewer components than the first scheme, we have made our initial test model a profiled horn, with an improved throat region. Unfortunatelly, despite the excellent performance of the new throat during the lab test, we also discovered a much higher level of mode conversion (from dominant mode to HE type higher order modes) inside the horn body than reported in [3]. The conversion is only within the HE group and is due to the wavefront curvature change. The copolar patterns are distorted and crosspolarization characteristics are not affected. We thus decided to pursue the conical horn plus phase corrector lens scheme, which is electrically equivalent to the profiled horn, while preserving the improved design for the throat region.

Since the size of the telescope field scales with wavelength at the secondary focus, while the feed horn field stays the same as frequency changes, in the final optics design we used another lens to refocus the telescope field to a tertiary focus. At the tertiary focus we obtain the image of the telescope aperture and the size of the beam waist is frequency independent. By choosing the proper feed horn aperture size the match between the telescope field and the feed horn field will also be frequency independent. This gives an aperture efficiency of about 84% across the band[5].

The new test model of the conical horn continued to show excellent performance in the throat characteristics, and this time it also produced the desired copolar radiation patterns. In what follows the details about the analysis and the design of the conical corrugated feed horns will be given, and the measurement results of the new conical horn and the current Hat Creek horns will be compared.

II. Fields in the Corrugated Waveguide

As mentioned in section I, we would like to produce the kind of boundary conditions which can support corrugated feed horn (more exactly corrugated waveguide) modes. In general these modes can be written as the superposition of the circular waveguide TE and TM modes of corresponding order traveling at the same longitudinal velocity. A discussion of the circular waveguide modes can be found in any standard microwave engineering text[6]. In a metallic wall circular waveguide of fixed radius, the TE and TM modes will in general have different phase velocities in the propagation direction, owing to their distinct transverse wavevelocities, required by the boundary conditions for the TE and TM cases. In order to equalize the transverse wave velocities, the TE and TM waves should effectively see different boundary conditions or surface impedances. This type of "anisotropic" boundary condition can be realized by azimuthally grooving the metallic wall, resulting the so called "corrugated waveguide". In what follows, a quantitative analysis of the fields in a corrugated waveguide will be given, through writing these fields as the superposition of TE and TM model fields and require them to satisfy the boundary conditions at the corrugated wall. The analysis follows mainly those given by Dragone [7,8].

Assuming cosΦ azimuthal variations, the fields inside a corrugated waveguide ($r \le a$) can be written as a superposition of a circular waveguide TE_1 and TM_1 modes (Fig.3):

$$
\begin{aligned}
E_z &= AJ_1(\kappa r)\cos\Phi e^{-j\beta z} \\
H_z &= \frac{1}{Z_0} BJ_1(\kappa r)\sin\Phi e^{-j\beta z} \\
E_\Phi &= \frac{j}{\sin\theta_1}\left[BJ_1'(\kappa r) + A\cos\theta_1 \frac{J_1(\kappa r)}{\kappa r}\right]\sin\Phi e^{-j\beta z} \\
H_\Phi &= \frac{1}{Z_0}\frac{-j}{\sin\theta_1}\left[AJ_1'(\kappa r) + B\cos\theta_1 \frac{J_1(\kappa r)}{\kappa r}\right]\cos\Phi e^{-j\beta z} \qquad (1) \\
E_\rho &= \frac{-j}{\sin\theta_1}\left[B\frac{J_1(\kappa r)}{\kappa r} + A\cos\theta_1 J_1'(\kappa r)\right]\cos\Phi e^{-j\beta z} \\
H_\rho &= \frac{-j}{\sin\theta_1}\left[A\frac{J_1(\kappa r)}{\kappa r} + B\cos\theta_1 J_1'(\kappa r)\right]\sin\Phi e^{-j\beta z}
\end{aligned}
$$

where

$$
\begin{aligned}
\kappa &= k\sin\theta_1 \qquad (2) \\
\kappa^2 + \beta^2 &= k^2
\end{aligned}
$$

and Z_0 is the free space wave impedance.

When the aperture size of the waveguide is large compared to wavelength (whereas the small aperture effects will be considered in the next section), higher space harmonics with $\beta = \beta_0 + \frac{2\pi N}{p}$, $N \geq 1$ can be ignored, i.e. we assume that β is a constant. When there is enough grooves per wavelength, the so call " surface impedance" approximation can be used. In this approximation, we assume that there are only TM (E_z, H_Φ, H_r) standing waves inside the slots and no TE type of standing waves. The bondary conditions become

$$E_\Phi = 0 \tag{3a}$$

$$\frac{H_\Phi}{E_z} = -\frac{1}{jX_s} \qquad \text{at } r = a \tag{3b}$$

where

$$jX_s = jZ_0 \tan(kd) \tag{3c}$$

and d is the depth of the groove.

Substitute the expressions for the fields (1) into the above boundary conditions, (3) becomes

$$\gamma \equiv \frac{A}{B} = -\frac{u}{\cos\theta_1}\frac{J_1'(u)}{J_1(u)} \tag{4a}$$

$$y \equiv -\frac{z_0}{X_s} = \frac{\cos\theta_1}{\sin\theta_1 u}\frac{1}{\gamma} + \frac{1}{\sin\theta_1}\frac{J_1'(u)}{J_1(u)} \tag{4b}$$

where $u \equiv ka\sin\theta_1 = \kappa a$.

Eliminating γ from the above two equations, we get

$$\frac{y}{ka} = \frac{1}{u^2}\frac{J_1(u)}{uJ_1'(u)}\left[\left(\frac{uJ_1'(u)}{J_1(u)}\right)^2 - 1 + \frac{u^2}{(ka)^2}\right] \tag{5}$$

For $ka >> 1$, $\theta_1 \approx 0$, and for u, y finite, this expression reduces to

$$\left(\frac{J_1'(u)}{J_1(u)}u\right)^2 - 1 = 0 \tag{6}$$

The two roots of the above equation are:

$$\frac{J_1'(u)u}{J_1(u)} = -1, \quad \text{or} \quad \gamma = 1 \quad \text{or} \qquad J_0(u) = 0 \tag{7a}$$

$$\frac{J_1'(u)u}{J_1(u)} = 1, \quad \text{or} \quad \gamma = -1 \quad \text{or} \quad J_2(u) = 0 \tag{7b}$$

Therefore for large ka, two sets of modes can exist inside the corrugated waveguide, corresponding to the solutions of the above two boundary equations:

$$HE_{1n} \text{ modes}, \quad u = u_{0n} \quad (n = 1,2,3\ldots) \text{ roots of } J_0 \tag{8a}$$

$$EH_{1n} \text{ modes, } u = u_{2n} \text{ (} n = 1,2,3... \text{) roots of } J_2 \tag{8b}$$

Thus when the boundary conditions (7) are satisfied we can write the transverse components of the fields in the corrugated waveguide as:

HE_{1n} modes

$$\vec{E}_t = -j\frac{ka}{u}A\left[J_0\left(\frac{r}{a}u\right)\hat{i}_x + \frac{1}{4}u^2\frac{y}{ka}J_2\left(\frac{r}{a}u\right)\left(\cos 2\Phi\hat{i}_x + \sin 2\Phi\hat{i}_y\right)\right]e^{-j\beta z} \tag{9a}$$

$$(u = u_{0n})$$

EH_{1n} modes

$$\vec{E}_t = j\frac{ka}{u}A\left[J_2\left(\frac{r}{a}u\right)\left(\cos 2\Phi\hat{i}_x + \sin 2\Phi\hat{i}_y\right)\right]e^{-j\beta z} \tag{9b}$$

$$(u = u_{2n})$$

What we would like for the aperture field of the feed horn is a smooth radial distribution, including a smooth taper at the edge of the aperture; a symmetric azimuthal distribution, and a single linearly polarized direction for the fields. From the field expressions we obtained for HE and EH modes (9a),(9b), we see that these features can only be achieved by the HE group of modes in the limit of $y/ka \rightarrow \infty$, and can never be achieved by the EH group of modes.

For the feed horns we normally use, the size of the waveguide near the aperture of the horn are usually big enough to support both type of modes. The only way to avoid the EH type of modes is not to excite them, or to cut-off these modes in the mode launching region of the horn. As for the modes within HE group, since the second term in the field expression (9) will introduce beam asymmetry and cross polarization, we need to have either $y \rightarrow 0$, which means the depth of the groove $d \rightarrow \lambda/4$, or $ka \rightarrow \infty$. In practice the first condition is usually satisfied at the center of the operation band by properly choosing the groove depth, and the second condition is approximated near the aperture for most of the aperture sizes we choose.

The mode dispersion diagram obtained from (2),(4) under the balanced hybrid condition ($\gamma = \pm 1$) is shown in Fig.4.

III. Design of the Mode Launching Region

From section II we learned that HE_{1n} modes could give us the desired circularly symmetric and linearly polarized beam. Specifically for our current test model, we are interested in generating only the HE_{11} mode, which has a pure $J_0(\kappa r)$ distribution over the aperture of the horn, with the first zero of J_0 lying on the boundary. Multi-HE-mode horn can be made by synthesizing a group of $J_0(\kappa r)$ distributions with different κ's. The bandwidth of the multi-mode horn is more limited than the single-mode horn, due the phase slippage of different modes inside the horn. It is also hard to excite

these modes to the correct ratio. The possibility of doing mode synthesis to improve aperture efficiency is still under investigation.

As mentioned before, for the usual aperture sizes in use both the HE and EH type of modes are supported. The only way to ensure single-mode operation is to design a mode launching region at the throat of the horn such that all the higher order modes are cut-off by the geometry of the throat. The mode launching region should have yet another equally important function, which is to achieve gradual transition from the impedance of a circular waveguide at the beginning of the throat to that of a corrugated waveguide at the end of the throat. All the mode selection and impedance matching functions have to be achieved over the entire frequency band of operation.

1. Throat Region Design for Single Mode Operation

First let us calculate the cutoff frequencies of various modes. From the two boundary conditions in (4), we get (without employing the approximation of $ka \to \infty$, since near the cutoff ka is usually small)

$$\gamma^2 + \gamma\omega - 1 = 0 \tag{10}$$

where

$$\omega = \frac{yu^2}{ka\cos\theta_1} \tag{11}$$

which has the solutions

$$\gamma_1 = \frac{-\omega + \sqrt{\omega^2 + 4}}{2} \tag{12a}$$

$$\gamma_2 = \frac{-\omega - \sqrt{\omega^2 + 4}}{2} \tag{12b}$$

These correspond to HE and EH modes in the limit of $ka \to \infty$ ($\gamma \to \pm 1$), respectively.

The condition for the cutoff of a mode is that its z direction propagation constant goes to zero, i.e. $\beta \to 0$ and $\cos\theta_1 = \beta/k \to 0$. For $y \neq 0$, according to (11) this will give $|\omega| \to \infty$. Therefore we obtain

$$\gamma_1 \to \begin{cases} 0 & \text{if } y > 0 \\ \infty & \text{if } y < 0 \end{cases} \tag{13a}$$

$$-\gamma_2 \to \begin{cases} \infty & \text{if } y > 0 \\ 0 & \text{if } y < 0 \end{cases} \tag{13b}$$

If $\gamma = 0$, this is a TE type cutoff (since γ is defined as the ratio of TM and TE modes). In this case, inside the main waveguide $H_z \neq 0$, $E_z = 0$, thus the surface reactance X_s has no effect on the cutoff. We can therefore replace the corrugated waveguide with a circular waveguide of radius a. The condition for the TE type of

cutoff is thus the same as that for a TE mode in a circular waveguide (with $\kappa \rightarrow k$ as $\beta \rightarrow 0$)

$$J_1'(ka) = 0 \tag{14}$$

If $\gamma = \infty$, the cutoff is TM type. The only nonzero z component of the field is E_z. If the disk making up the groove is thin, the fields can penetrate inside the slot region. Therefore we can replace the corrugated waveguide with a circular waveguide of radius b. Thus the condition for the TM type of cutoff becomes

$$J_1(kb) = 0 \tag{15}$$

In fact, whether in the cutoff region the field can penetrate the slots or not can also be seen quite intuitively from the TE and TM field distrabutions inside the circular waveguide (Fig.5). For TE wave, since the H field (dashed lines) has longitudinal component, the boundary condition will prevent it from penetrating into the slots, we thus have r = a is the radius of the corresponding waveguide. For TM case, the magnetic field has no longitudinal component, both E and H field can penetrate inside the slots in the cutoff situation. Therefore the corresponding waveguide radius is r = b.

When $y = 0$, $\gamma = \pm 1$. From boundary condition relation (4), i.e.

$$\gamma = -\frac{u}{\cos\theta_1}\frac{J_1'(u)}{J_1(u)} \tag{16}$$

we must have $J_1'(ka) = 0$ for $\cos\theta_1 = 0$. Both type of modes have the same cutoff.

Besides, when $y < 0$, there can also exists a surface type of mode which is again undesirable. In practice we choose our dimensions in the throat such that we always have $y > 0$.

From the above discussions we get the following mode diagram. (Fig.6). Several mistakes have been corrected compared to the original mode diagram given by Dragone[8]. In principle we would like to cutoff all the modes besides HE_{11}. In practice EH_{11} can be allowed inside the throat since, from looking at the mode dispersion diagram in Fig.4, we see that as ka increases the β corresponds to EH_{11} decreases to zero. This means that even if we excited some EH_{11} mode in the beginning, it will die off as ka gets larger inside the throat region.

The region for HE_{11} only propagation (ignoring the EH_{11} mode) is indicated by the shaded area. The maximum range of single-mode-operation choice corresponds to the part of the double-dashed line inside the shaded region, which gives a specific choice of the initial groove dimensions a and b for a given frequency range. To determine the size of a we need also to consider the requirement in the circular waveguide section (see Appendix for details of the choice of a). This later consideration will in general give an a value not very different from that dertermined by the first consideration alone. The corresponding b is determined by compromising between placing the

operation points close to the optimum b/a line, and placing the highest frequency operation point as close as possible to the boundary of the single-mode region, so as to achieve the maximum bandwidth in a design. This will in general give a $d = b - a \approx \lambda_{0h}/2$, where λ_{0h} is the free space wavelength at the highest operation frequency. These choice of a,b at the beginning of the throat will give a single-mode operation range of about 50%, which is just enough to cover our 70 - 115 GHz bandwidth. The throat will gradually flare the depth of the grooves from $\lambda_{0h}/2$ to $\lambda_{0c}/4$ (where λ_{0c} is the free space wavelength at the CENTER of the operation band) over a distance of several wavelength, to ensure gradual transition of surface impedance and the cutoff of higher order modes. In our design, this flare of groove depth is realized by changing the the parameter a only, while keeping b always constant inside the throat. As we move along the throat region, the operation points will move on the mode diagram (Fig.6) along a series of horizontal lines starting from the points on the line $\omega_1\omega_2$. This type of throat design generally gives the widest physical range of single-mode propagation while we move within the throat region. The schematics for the throat design according to the single-mode requirement alone is shown in Fig.7.

2. Impedance Matching Considerations

The mode launching region, or the "throat", should act at the same time as an impedance transformer, which gradually transforms the field distribution inside a circular waveguide to that of a corrugated waveguide (Fig.8). This is realized by a smooth transition of the boundary conditions.

The theory of transmission lines tells us that a uniform transmission line of length d can transform the terminal impedance to the input port in a way such that $Z_{in} = Z_t \tan kd$. This tells us that a transmission line of length $d = \lambda/2$ will exactly reflect the terminal impedance to the input port. This relation suggests that a slot depth of $\lambda/2$ will effectively create the same surface impedance as the perfect metal wall. It seems that our previous choice of the throat design for single-mode operation will fit naturally for the impedance matching purpose. This point is in fact also hinted in Dragone's monumental papers[7,8].

Unforturnately this is not usually true. The reasons for this are two fold. First of all, to treat the slots as perfect transmission lines, or to use the impedance transformation relation

$$Z_{in} = Z_t \tan kd \tag{17}$$

we have to be in the regime $ka \gg 1$, and $kh \ll 1$ (where h is the spacing between grooves). When we have only finite number of grooves per wavelength and are in the region of small ka, as in the throat, the value of d used in the impedance transformation formular usually needs to be corrected. Secondly, the surface impedance on the corrugated surface do not exactly equal to Z_{in} due to the the finite thickness of the disks. In the case of sufficient grooves per wavelength, the effect of the disks can be accounted for by introducing an effective surface impedance

$$Z_s = jX_s = Z_{in}(1 - \frac{t}{h}) \qquad (18)$$

where t is the thickness of the disks. From equation (18) it is clear that when we try to create an resonant slot with $X_s = \infty$ using a $\lambda/4$ groove, we will have much less frequency sensitivity if we have small t/h, i.e. thin disks compared to groove spacing. This choice of t/h, as we will show, which is necessary for the grooves of the main horn body, makes the effect of the length correction in the impedance transformation formulas (17),(18) much more prominent in the limit of small ka. The overall effect of these complications is that a groove depth of $\lambda_{0h}/2$ at the beginning of the throat will in general fail to give a surface impedance of 0, and in many cases the value of impedance it gives is close to ∞, as can be seen below.

The effect of small ka, finite number of grooves per wavelength, and the effect of the ratio of t/h can be rigorously treated by including all the space harmonics and solving the corrugated waveguide as a periodic structure[4]. One example of the result of this calculation is shown on Fig.9. Careful observations of this figure show that the guide wavelength in the slots increases for smaller ka and for small value of t/g (or t/h). In the design we will eventually use (section V), the choice of initial ka corresponds to $D/\lambda \approx 0.8$. When we choose to use t/g = 1/2, with g = 0.2λ, as for the main horn body, the $\lambda_{0h}/2$ choice of our beginning slot corresponds to roughly $\lambda_g/4$ in terms of guide wavelength. So instead of achieving $X_s = 0$ what we actually get is $X_s = \infty$, which is still the boundary condition of the corrugated wall. This certainly will fail to function as the desired impedance transformer. Further increase in the slot depth will make our other goal of wideband single-mode operation unattainable.

The way to get around this difficulty comes again from the hint given by Fig.9. We see that in the case of small ka, an increase in the value of t/g (disk width/ groove width) alone will bring the guide wavelength back to the corresponding free space value. This suggest that if we flare both the width and the depth of the slots, i.e. to use longer ($\lambda_{0h}/2$) AND thinner (t/g = 7) slot in the beginning of the throat, gradually change it to shorter ($\lambda_{0c}/4$) and wider (t/g =1/2) slot, we will be able to achieve both the impedance matching and mode selection functions. This is exactly what we choose to use in our design of the new feed horn (Fig.10).

This way of varying both the groove depth and groove width simultaneously to achieve wideband single-mode operation and wideband impedance matching, although occasionally appeared in the literature[9] as an emperical way for designing the mode launching region (since it's natural in microwave design to make any kind of transitions as smooth as possible), is not present in most of the corrugated feed horn mode launcher designs. The reason, the author believes, is because the guide-wavelength variation effect at small ka, and the necessity of using space harmonics to obtain rigorous result and to adjust the design parameters correspondingly, have never been fully understood and appreciated by most of the designers (For example, this was mistreated in the Dragone's otherwise excellent papers of 1976 [7,8]. The most complete corrugated feed horn text of Clarricoats and Olver[4], although included the space harmonics analysis in sections of their book, nontheless did not make use of this

knowledge in their mode launching region section. They still mistakenly used the free space wavelength in the impedance transformation relations. The return loss results of these designers are therefore generally poor). Very likely even the people who emperically applied this scheme did not realize, on a theoretical basis, why tapering both in the width and in the depth of the grooves gave a better wideband matching!

IV. Choice of the Conical Flare Angle, Aperture Size and the Groove Dimensions

After launching the desired HE_{11} mode in the throat, we would like to design a feed horn flared section with the appropriate outer dimensions and groove size such that HE_{11} mode will propagate to the horn aperture without significant mode conversion into higher order modes. Under single-mode operation the crosspolar characteristics are determined mainly by the groove dimensions, while the copolar radiation characteristics by the aperture size and flare angle.

1. Mode Conversion in a Small Flare-Angled Conical Horn

By assuming $ka >> 1$, $y \approx$ constant and for small flare angled horn, Dragone [7] derived that between two locations along the horn axis $z = z_1$ and $z = z_2$, the converted EH_{11} mode power P_c has the following value compared to the incident HE_{11} power P_0

$$P_c = P_0 \times 3.393(10^{-3}) y^2 \tan^2\alpha \, | \, 1 - e^{j\psi} \, |^2 \tag{19}$$

where

$$\psi = \frac{10.295}{y \tan\alpha} \frac{y}{ka(z_1)} \left[1 - \frac{a(z_1)}{a(z_2)} \right] \tag{20}$$

and α is the flare angle. Therefore,

$$P_c = P_0 \times 1.357(10^{-2}) y^2 \tan^2\alpha \tag{21}$$

For $y = 1$,

$$\frac{P_c}{P_{0\,\alpha = 4^\circ}} \approx -42\text{dB} \tag{22a}$$

$$\frac{P_c}{P_{0\,\alpha = 16^\circ}} \approx -29.8\text{dB} \tag{22b}$$

Therefore if we keep the feed horn flare angle less than 15°, and do not operate far from the slot resonance, so that y is not very large, the mode conversion will be small.

2. Determine the Groove Dimensions for the Crosspolar Radiation Characteristics

For a small flare angled conical horn, mode conversion along the feed horn is usually small. The crosspolar radiation characteristics is determined mainly by the intrinsic crosspolar radiations of the dominant HE_{11} mode.

We have derived in section II that for a corrugated waveguide of radius a the electric field due to HE_{11} mode can be expressed as

$$\hat{E} = AJ_0(\kappa r)\hat{i_x} - \frac{X - Y}{4}\frac{u_0^2}{ka}J_2(\kappa r)(\cos 2\Phi \hat{i_x} + \sin 2\Phi \hat{i_y}) \qquad (23)$$

where $X \approx E_\Phi/H_z$, $Y \approx H_\Phi/E_z$ at the boundary.

We see from the above field expression that if we want to reduce the value of the second term, which accounts for the beam unsymmetry and crosspolar radiations, we can either make X - Y = 0 (grooves at resonance) or $ka \rightarrow \infty$ (large aperture size).

The aperture size is usually determined by the copolar radiation and telescope optics considerations. For a fixed aperture size the crosspolar radiation characteristics changes with frequency due to the change in surface impedance. Usually the slot depth is chosen such that the resonance occurs near the center of the operation band. The bandwidth characteristics of the crosspolarization levels for different aperture sizes are given in Fig.11.

The groove spacing is chosen such that the it satisfies the fabracation and cost constraint, and yet it is fine enough to satisfy the surface impedance approximation. Tests on the groove coarseness effect have been carried out using a program package CWGSCAT[10] which model the horn by cascading the cylindrical sections of the grooves and ridges to obtain the total scattering matrix of the feed horn. The results of these tests, all of them done at 90 GHz, are given in Fig.12. We see that the 3 groove per wavelength results are almost identical to to 6 groove per wavelength results, with the slight difference in the E and H plane patterns caused by the intrinsic HE_{11} radiations (23). As the number of grooves decreases the E and H plane patterns differ more and more, indicating the invation of higher order modes. It is generally safe in a design if we stay above 2.3 grooves per wavelength at the high end of the operation band. Our later choice of groove spacing corresponds to 3 grooves per wavelength at the band center and 2.5 grooves per wavelength at the higher frequency end.

3. Choice of Aperture Size and Horn Flare Angle for Copolar Radiation Characteristics

The radiation patterns of a corrugated feed horn can be determined from the Fourier transform of the aperture field distributions. For feed horns with large enough aperture size and moderate flare angle, the aperture field is mainly of the form of a truncated J_0 amplitude distribution, and a second order spherical cap phase distribution. The exact form of amplitude distribution has been derived in section II, for HE_{11}mode it is given by (23). The phase distribution can be derived as follows.

Assuming approximate azimuthal symmetry, a condition which holds near the resonance of grooves, the electric field on the aperture can be written as the product of an amplitude and a phase distribution (Fig.13)

$$E = f(r)e^{jg(r)} \tag{24}$$

where f(r) is the amplitude distribution given by (23), and

$$g(r) = \beta(R(r)-R_1) \tag{25}$$

is the phase distribution relative to the center of the aperture, and β is the propagation constant of HE_{11} mode. $\beta \approx k_0$ for large enough aperture size. From Fig.13,

$$R(r) = (R_1^2+r^2)^{1/2} = R_1[1 + (\frac{r}{R_1})^2]^{1/2} \tag{26}$$

$$\approx R_1[1 + \frac{1}{2}(\frac{r}{R_1})^2] \tag{27}$$

Therefore

$$g(r) \approx \frac{1}{2}\beta\frac{r^2}{r_1} \tag{28}$$

The far field patterns can be calculated through the Fourier transform of the aperture field (24). The gereral results of these far field calculations for different flare angles are given in Fig.14. In the special case of a flat phase front, analytical expressions for the far fields are also available[8], i.e.

$$F = N_0(u,v)\hat{i}_x + \frac{\gamma-1}{\gamma+1}N_2(u,v)(\cos2\Phi\hat{i}_x + \sin2\Phi\hat{i}_y) \tag{29}$$

where

$$v = ka\sin\theta \tag{30}$$

and

$$N_k(u,v) = \frac{a^2}{v^2-u^2}[vJ_k(u)J_1(v) - uJ_k(v)J_1(u)] \tag{31}$$

Using either the aperture field or the far field to overlap with telescope field at corresponding positions, the aperture efficiencies over the frequency band for a specific choice of aperture size can be calculated. This allow us to determine an optimum choice of the aperture size for different optics configurations.

The conical flare angle has an added effect of causing reflactions at the end of the throat, because this is a discontinuity if the flare angle at the throat and at the horn body are different. This effect is also tested using the program CWGSCAT, also done at 90 GHz, and the results are summarized in Fig.15. Our final choice of 12 degree flare angle clearly placed us in a save region.

V. Design Procedure and the Measurement Results on the New and Old Conical Horns

The test model for the new conical horn is intended to work with the upgrading new receivers, which have 3 operation bands: 70 - 90 Ghz, 85 - 115 Ghz and 210 - 270 Ghz. The parameters chosen for this model is for the 85 - 115 Ghz band horn. Horns for other bands can be designed by simple scaling plus some minor changes in the throat. Since besides working on the new receivers we are also interested in fixing up the problems with the horns on the existing antennas, the parameters for the final design of the new conical horn is so chosen that it actually works from 70 to 115 Ghz, to allow the possibility that we might install it on the existing antennas. The groove depth is nonetheless optimized around 101 Ghz, the center of the new band.

The schematics and the parameters for the new conical horn are shown in Fig.2, Fig.10 and Fig.16. The input surface has the inner cross-section of a WR-10 waveguide and it flares gradually into a circular waveguide. The dimension of the WR-10 waveguide has the standard value of 0.05" by 0.1", which can support the rectangular waveguide TE_{10} mode in the 70 - 115 Ghz range. The procedure to determine the radius of the circular waveguide near the end of the transition section is discussed in the Appendix. The final choice of radius a = 0.061" allows only the circular waveguide TE_{11} mode to propagate.

The a = 0.061" circular waveguide connects to the mode launching region or "throat" of the feed horn. The throat consists of 11 grooves of varying depth and width, with the pitch of the grooves being uniform and equals to the value used for the main horn body, i.e. h=0.0394". This value is about 1 groove per millimeter or 3 grooves per wavelength near 100 Ghz. The first groove has a depth of d_0 = 0.0507", corresponds to $\lambda_0/2$ near 115 Ghz. This choice of initial a_0 and $b_0 = d_0 + a_0$, with b_0/a_0 = 0.1117/0.061 ≈ 7.0155/3.8317, corresponds to operation points on the straight line in the mode diagram(Fig.6), with 115 Ghz point near the top of the intersection of the line with the single-mode region (ω_1) and the 70 GHz point near the bottom the intersection of the line with the single-mode region (ω_2), as we vary the frequency. The very large ratio of the initial disk width versus the groove spacing, i.e. t_0/g_0 = 0.0344/0.005 ≈ 7/1, makes the value of the guide-wavelength inside the slot approximately that of the free space wavelength. This makes it possible to for us satisfy both the wide band single-mode operation and wide band impedance matching requirements using the same set of throat parameters, as demonstrated in section III. The grooves then flare linearly both in depth and width to their values for the main body of the horn at the end of the throat, i.e. t/g = 1/2. In the throat region the b value or the outer radius at the bottom of the grooves is kept constant till the end of the throat, so that the operation points move horizontally in our mode diagram (Fig.6) as we move along the throat, keeping the maximum physical distance of single-mode propagation, to ensure that higher order modes have enough distance to decay.

As stated in section IV, the groove dimensions for the main horn body were chosen to achieve the desired crosspolar radiation characteristics. The groove depth d = 0.029" is chosen such that it is resonant near the center of the operation band 85 - 115 Ghz, i.e. 101 Ghz. The choice of groove spacing h = 0.0394" corresponds to 3 grooves per wavelength near 100 Ghz. The numerical simulations in section IV show that this groove coarseness is enough to ensure HE_{11} mode propagation without converting it into higher order modes, which happens when the the surface impedance approximation breaks down. The ratio of ridge width to groove spacing should be made as small as possible theoretically to reduce the frequency sensitivity of the crosspolar radiation characteristics. In practice this ratio is limited by the electroforming process. As a compromise a value of t/h = 0.33 or t/g=0.5 has been used.

The flare angle of the horn has been chosen to be 12 degrees to place it within the category of small flare-angled horn. The conical horn flares to an aperture size of a = 0.3507", determined by the optics considerations of the new system. This gives a total length of the feed horn (rectangular-to-circular transition section + throat + horn flare) of 2.6942". There are altogether 43 grooves.

The design as shown in Fig.2,10,16 was sent to the Custom Microwave Co., Colorado to be electroformed, and after we received it a set of measurements were made at the lab in Berkeley. The results were then compared with the theoretical calculations, and with the measurement results for the old Hat Creek horns.

The measured copolar radiation patterns of the new conical horn at 90 Ghz is shown in Fig.17. Pattern symmetry is observed between E and H plane patterns, which indicate these are single-mode fields. The copolar patterns are then averaged and plotted in Fig.18 on a different scale, to ease the comparison with the theoretical results. From this plot the agreement between theoretical prediction and the measurements is obvious. Similar agreement at other frequencies are also observed.

The measured return loss for the old and the new horns are given in Fig.19. Over most of the frequency range the return loss have improved from -17dB to -30dB. The oscillations observed on the return loss plot for the new horn are believed to be due to the internal reflections of the slotted line used for measuring the standing waves. The performance at the high frequency end for the new horn is also limited by the measuring instrument's internal reflections. The true values are expected to be even better.

The measured crosspolarization levels of the old and the new horns are given in Fig.20. These levels are measured on a plane 45 degrees in between E and H planes, which in general gives maximum values of the crosspolarization. The peak level of the crosspolarization on this plane is searched, and then compared with the copolar peak to get the relative dB values. The high values of crosspolarization of the old horn beyond 105 Ghz indicates the emerging of higher order EH modes. This can also be realized from the asymmetry of the copolar radiation patterns of the old horn, which will be given in the next section.

The comparisons of the measurement results between the new and old conical horn, and with the theoretical results, show that the new conical horn gives a big level of improvements over the old model. The degradation of the old horns at high frequencies accounts at least in part for the drop in aperture efficiency at higher frequencies in the existing system, as the calculations in the next section will show.

VI. Investigations on the Old Hat Creek Horns and Optics, Preparation for the Retrofit of the Existing System

The analysis and the measurement results of the previous sections show that the old design of the Hat Creek horns is multi-moded at high frequencies. To quantitatively determine the onset of the multi-modedness and its effect on the aperture efficiency of the existing system, a series of calculations have been done starting from the dimensions on the old horn drawings.

The program used in this calculation is again the CWGSCAT package. Fig.21 - 24 show the calculated amplitudes and phases of the old horn at 90 GHz and 115 Ghz. It can be seen that the 90 GHz pattern is circularly symmetric but the 115 GHz pattern is not symmetric. These calculations confirm our previous conclusion that the old horn at high frequency is multi-moded. Similar calculations across the frequency band show that the multi-modedness starts around 108 GHz, and gets serious after 110 GHz. The calculated beam patterns in Fig.21 and 23 also agree with the holographic measurements of the beam patterns on the sky, shown in Fig.25 and 26. The 113 GHz pattern is clearly much more asymmetrical than the 90 Ghz pattern.

Having obtained the E and H plane patterns, a set of formulas can be used[11] to calculate the aperture efficiencies due to the contributions of spillover, phaseloss, illumination and crosspolarization, respectively. The results of these calculations are summarized in the plots in Fig.27. It can be seen that the horn starts to become multi-moded around 108 GHz. There is in general a dip in almost all the curves (except for the illumination efficiency, which gets better as the spillover gets worse). The reason for the dip is because that after the horn becomes multi-moded, different modes slip in phase inside the horn due to their distinct propagation velocities. The amount of the phase slippage when the modes arrive at the aperture of the horn varies with frequency. At certain frequency the synthesized pattern will be the poorest. The fact that this dip seem to happen around 110 GHz instead of 115 GHz, as in our real system, is probably due to the machining errors of the old horns (only a few mils of error is enough to shift the frequency by this much). The little peak inside the dip of the phaseloss efficiency curve is due to the fact that as we increse the frequency from the left side of the dip, different modes change their relative phases as the frequency changes. At this particular frequency, the E and H plane patterns, thus also the phase patterns, temporarily overlap and then, as frequency increases further, will separate in an opposite way (i.e. below this frequency the E plane pattern is wider than the H plane pattern, whereas after this frequency the H Plane pattern gets wider).

When we multiply the four efficiency curves on Fig.27, and also incorporate the return loss result of Fig.19 (assuming a return-loss value of 1% for f < 110 GHz, and a return-loss value of 5% for f ≥ 110 GHz, for simplicity), we obtain the overall theoretical aperture efficiency of this multi-moded feed horn, as plotted in Fig.28. Also plotted on the same figure is the theoretical efficiency of a horn with the same dimensions except that the throat has a single-moded design. This later curve is the best that the old Hat Creek optics design can achieve, provided that the horn performs ideally. This number, 72-74% across the band of 70-115 GHz, can be improved to 78-82% over a 30% bandwidth if we use a phase corrector lens in the aperture of the horn, with a different choice of the aperture size. The number can be further improved to 84% by placing the horn and the phase corrector lens at the tertiary focus of the telescope through the use of a tertiary lens (Fig.29). The match of the telescope field and the feed horn field for the tertiary design will be frequency independent[5].

The calculations and measurements encouraged us to retrofit the new feed horn and optics on the existing system. The tertiary and secondary theoretical aperture efficiencies are plotted on Fig.30, together with the calculated efficiencies for the old Hat Creek horn. These efficiencies do not include the feed-leg blockage or surface Ruze loss, which will have the same effect on all types of designs. From this plot we can see that at the high frequency end where the dip happens we can expect at least a factor of 1.4 improvement due to the feed horn and optics upgrade. This number can be even bigger if we consider the fact that the circular waveguide in the old rectangular-to-circular transition section design, with a = 0.0625" instead of the new value a = 0.061", was also multi-moded at higher frequencies.

The retrofit of the existing system was planned and prepared in May and June 1991. By the time this memo is finished, we have actually installed the new horn plus 2 lenses on antenna 1. Similar retrofit will be done for antennas 2 and 3 soon. The results of these retrofits will be summarized in a separate memo.

Appendix. Design of the Rectangular to Circular Waveguide Transition Section

The mode launching region (throat) of the feed horn acts as a smooth transition between a corrugated waveguide and a circular waveguide, whereas the standard connection to the mixer block input is a rectangular waveguide. A further rectangular-to-circular waveguide transition section is therefore needed to achieve smooth connection between these two types of waveguides.

The rectangular waveguide used for the 70 - 115 GHz band is of the type WR–10, which has the cross section dimension a = 0.1" and b = 0.05". For rectangular waveguide TE_{mn} modes, the cutoff frequency has the following general expression

$$f_c = \frac{\sqrt{(\frac{m\pi}{a})^2 + (\frac{n\pi}{b})^2}}{2\pi c} \qquad \text{(A1)}$$

At any frequency (and their corresponding wavelength) only modes with cutoff frequency smaller (or cutoff wavelength bigger) than the operating frequency (or wavelength) can propagate. Using the dimensions of WR–10 waveguide in this formula, we see that TE_{10} mode has a cutoff frequency of 59 GHz, where as all the other TE_{mn} modes have cutoff frequencies above 115 GHz. Therefore TE_{10} is the only mode that can exist in the WR–10 waveguide in the 70 to 115 GHz frequency range, which is also the mode we would like to use. The field distributions of rectangular waveguide TE_{10} mode can be found in any standard microwave text, such as in [6].

The dimension of the circular waveguide is chosen so that the circular waveguide TE_{11} mode can propagate (since this is the mode who's field distribution forms a most natural transition between rectangular waveguide TE_{11} mode and corrugated waveguide HE_{11}mode), whereas most of the other modes are either cutoff by the circular waveguide dimensions or impossible to be excited due to the symmetry of the waveguide.

The cutoff wavelengths for the circular waveguide TE_{ni} and TM_{ni} modes have the following expressions

TM modes

$$(\lambda_c)_{TM_{ni}} = \frac{2\pi a}{\mu_{ni}} \tag{A2}$$

where μ_{ni} is the ith root of nth order Bessel function, c is the velocity of light in free space, and

TE modes

$$(\lambda_c)_{TE_{ni}} = \frac{2\pi a}{c\nu_{ni}} \tag{A3}$$

where ν_{ni} is the ith root of the first derivative of the nth order Bessel function.

Using these formulas, the cutoff wavelengths can be calculated and they are plotted on Fig.31. Our operation range of 70 Ghz and 115 GHz corresponding to λ in the range of 4.28mm and 2.6mm. With a chioce of circular waveguide radius a = 0.061" = 1.55mm, The corresponding λ will be in the range of 1.68a and 2.77a. In this region, the only propagating modes are TE_{11}, TM_{01}, and TE_{21}. Among them the first one is the desired working mode and the second and the third have the field symmetry which do not couple energy from rectangular TE_{11} mode. This choice of a is mainly to cutoff the most harmful TM_{11} mode, while still keeping the size of the circular waveguide large enough to reduce metal loss.

The final choice of the dimensions for the rectangular to circular waveguide transition section is shown in Fig.16. Small sections of rectangular and circular waveguide attached at each end of the transition section are for the purposes of securing both the smooth transition and the higher order mode cutoff.

Acknowledgement

My work on the design and test of the corrugated feed horns could not have completed without the help and encouragement of many others. I would like to thank Mr. Emory Horvath and the Custom Microwave Co. for fabricating an excellent model of the feed horn which matches the design beautifully. Thanks for Dan Hoppe at JPL for providing us the CWGSCAT program package for modeling the feed horns. I thank my advisor Jack Welch for assigning me this interesting project for part of my thesis research. I thank the people in the Radio Astronomy Lab in Berkeley, especially people in the receiver group, for their ever lasting interests in my progress, for their continued support and help. Special thanks for Jan Tauber, Dick Plambeck and John Lugten who helped be with the initial setup of the measurement scattering range, and who skillfully repaired some of the broken instruments used in the tests. Thanks to John Lugten, Jerry Hudson and Jack Welch for many interesting discussions on optics and feed horns. Thanks to Dick Plambeck and William Holzapel for providing the holograpy measurement plots used in this memo.

References

[1] M. A. Janssen, S. M. Bednarczyk, S. Gulkis, H. W. Marlin and G. F. Smoot, " Pattern Measurements of Low-Sidelobe Horn Antenna," *IEEE Trans. Antennas Propagat.*, vol. AP-27, No.4, pp. 551-555, July 1979.

[2] G. L. James, "Analysis and design of TE11-to-HE11 corrugated cylindrical waveguide mode converters," *IEEE Trans. Microwave Theory Tech.*, Vol. MTT-29, pp 1059-1066, 1981

[3] S. F. Mahmoud, "Mode conversion on profiled corrugated conical horns," *Proc. IEE,* Vol. 130, Pt. H., No. 6, Oct. 1983

[4] P.J.B.Clarricoats and A.D.Olver, " Corrugated Horns for Microwave Antennas," *London, UK: Peter Peregrinus, 1984*

[5] R.Padman, J.A. Murohy and R.E. Hills, " Gaussian Mode Analysis of Cassegrain Antenna Efficiency," *IEEE Trans. Antennas. and Propag.* Vol. Ap-35, No 10, Oct. 1987

[6] N. Marcuvitz, " Waveguide Handbook," *London, UK: Peter Peregrinus, c1986*

[7] C. Dragone, " Reflection, transmission, and mode conversion in a Corrugated feed," *Bell System Tech. Journal,* July-August 1977, pp 835-867

[8] C. Dragone, " Characteristics of a broadband microwave corrugated feed: a comparison between theory and experiment," *Bell System Tech. Journal,* July-August 1977, pp 869-888

[9] P.F.Goldsmith, " Quasi-Optical Techniques at Millimeter and Submillimeter Wavelengths," in *Infrared and Millimeter Waves* Vol. 6, Ch.5, 1982

[10] D. Hoppe, "CWGSCAT", a program package developed at JPL, and distributed by COSMIC. Co.

[11] B. MacA. Thomas, "Theoretical performance of prime-focus paraboloids using cylindrical hybrid-mode feeds," *Proc. IEE* Vol. 118, pp 1539-1549, Nov. 1971.

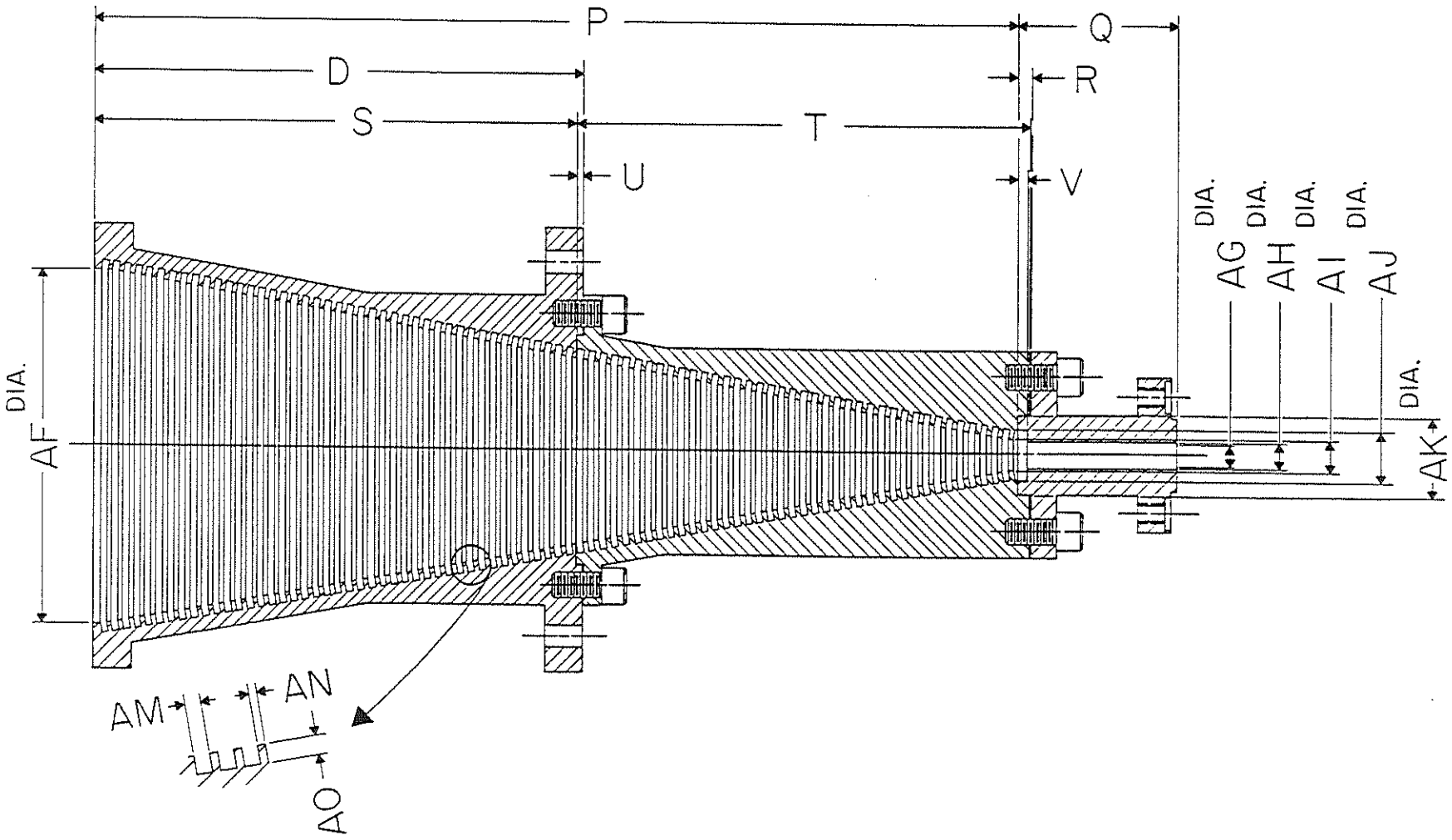

Figure 1. Design Layout for the Old Hat Creek Horns

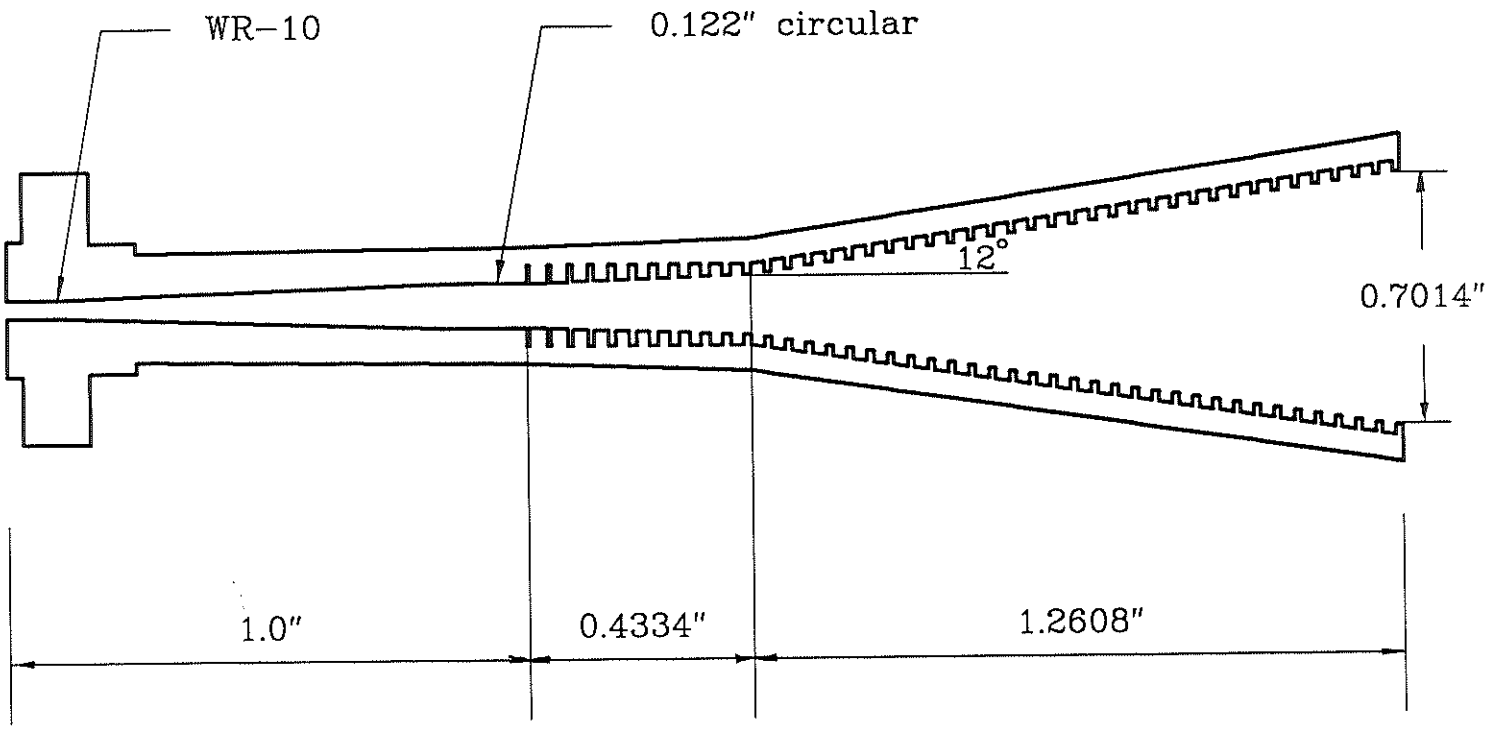

Figure 2.Design Layout for the New Conical Horn

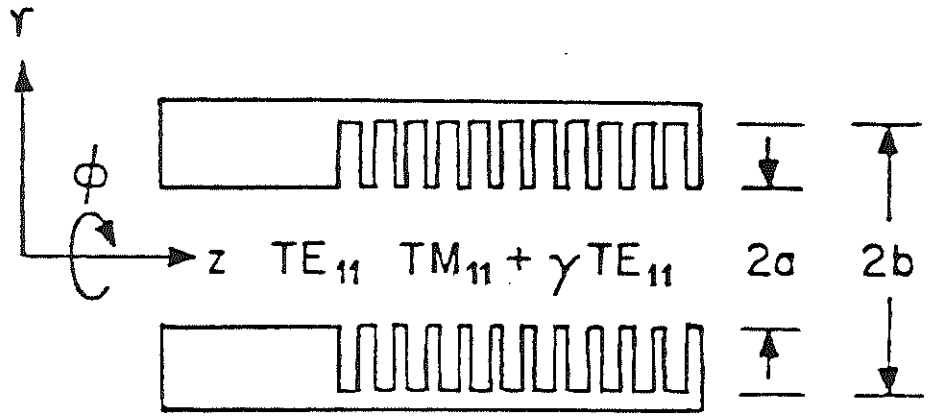

Figure 3. Corrugated Waveguide

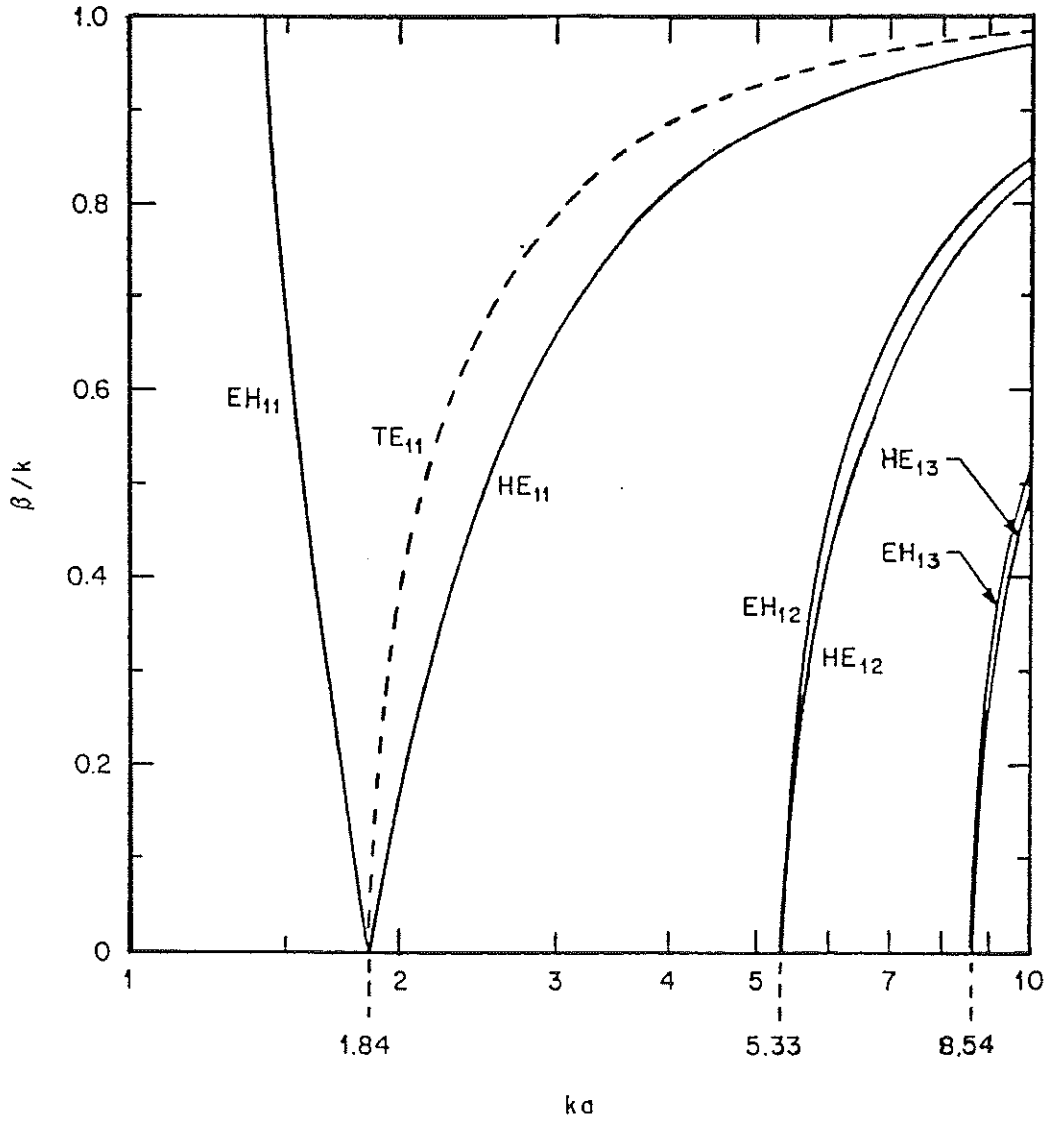

Figure 4. Dispersion Diagram for the Corrugated-Waveguide Modes Under the Balanced Hybrid Condition ($\gamma = \pm 1$). TE_{11} Mode Also Shown for Comparison

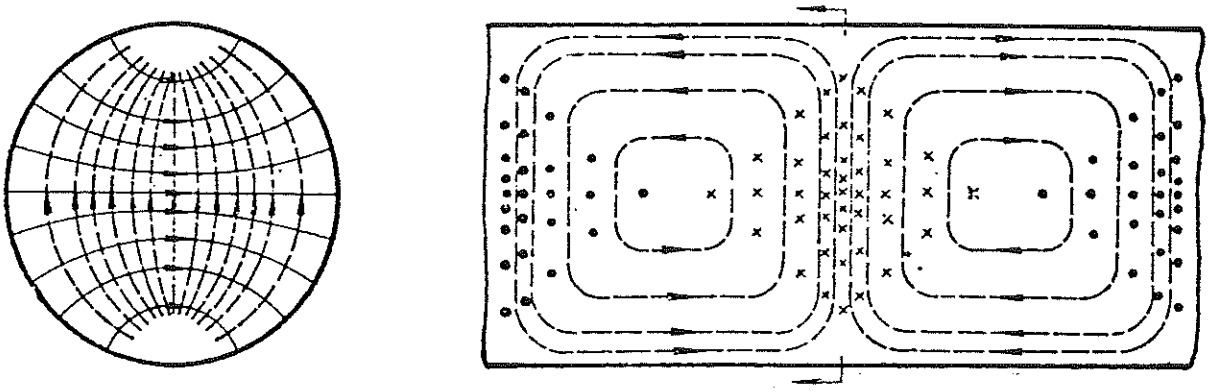

TE_{11}

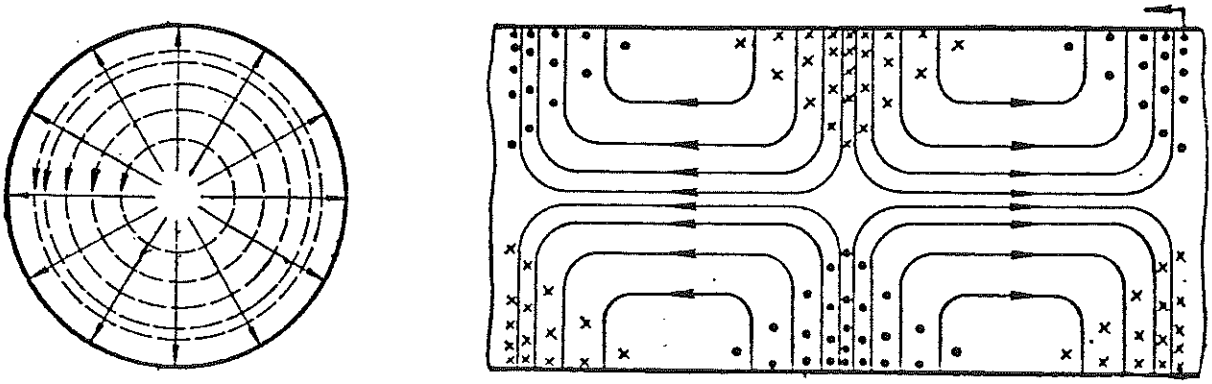

TM_{01}

Figure 5. Circular Waveguide Modal Fields: TE_{11} and TM_{01} Modes

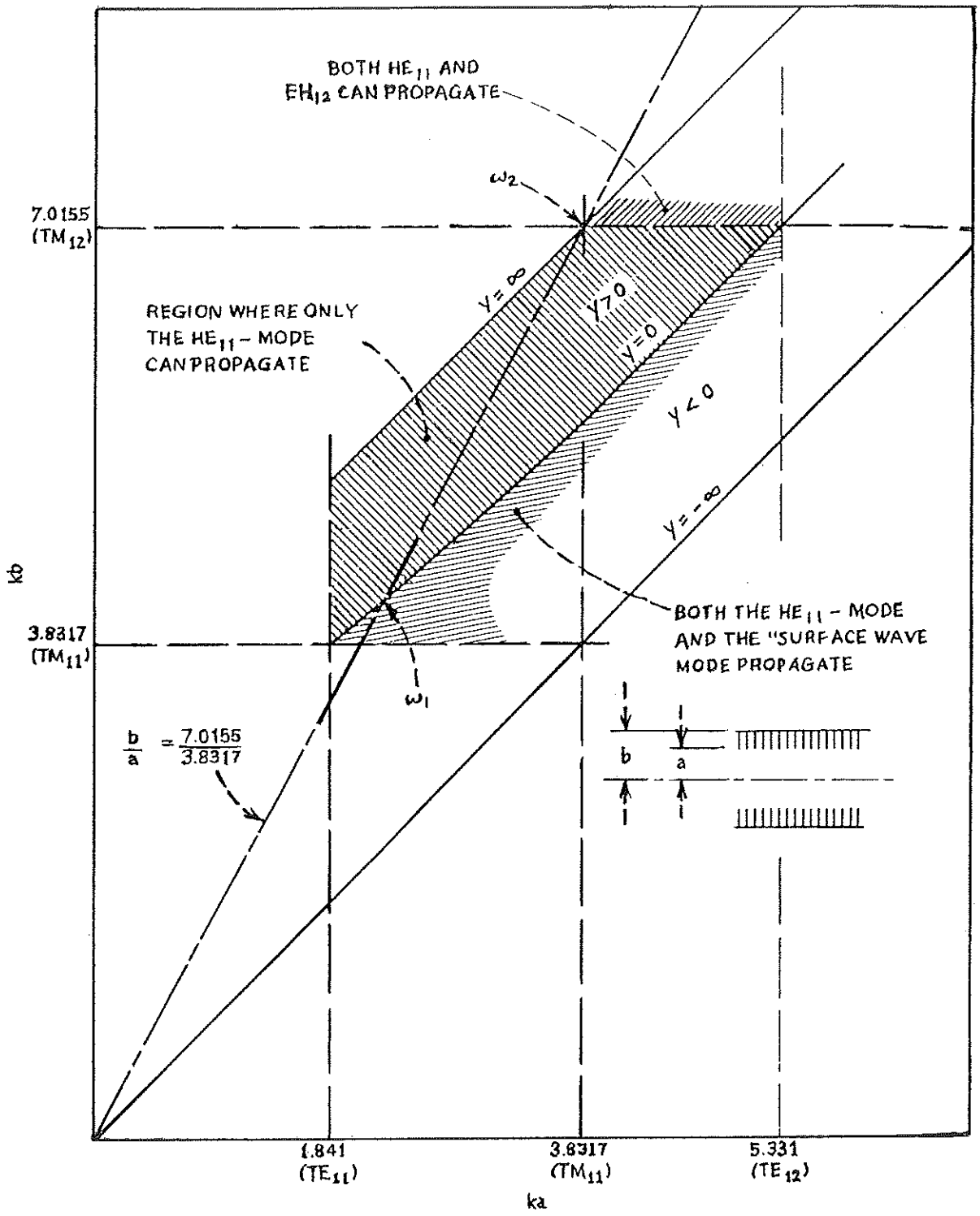

Figure 6. Mode Diagram for Corrugated Waveguide

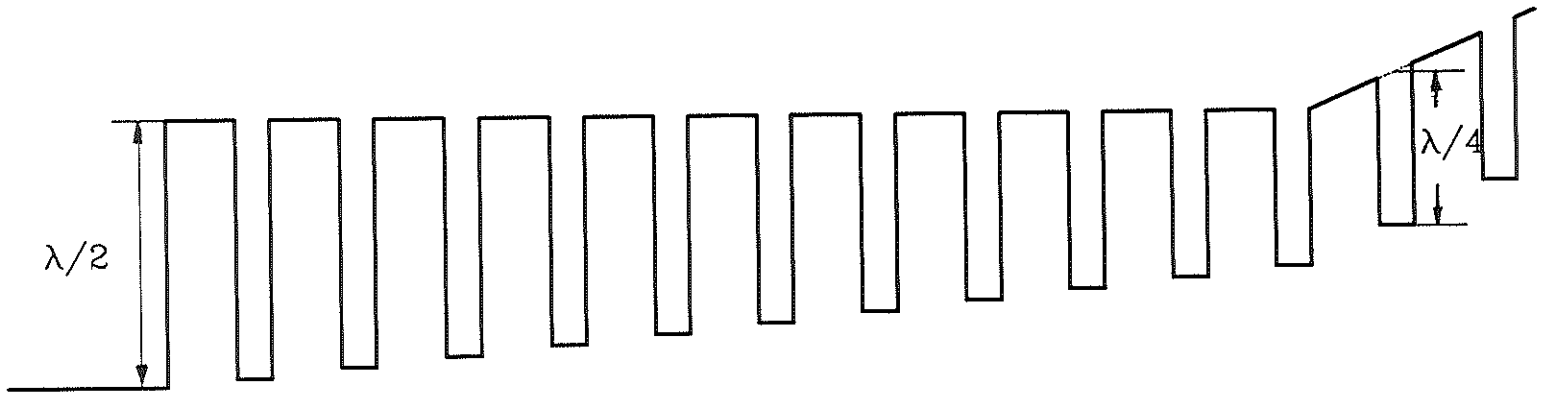

Figure 7. Possible Choice of the Throat Design for Single Mode Operation

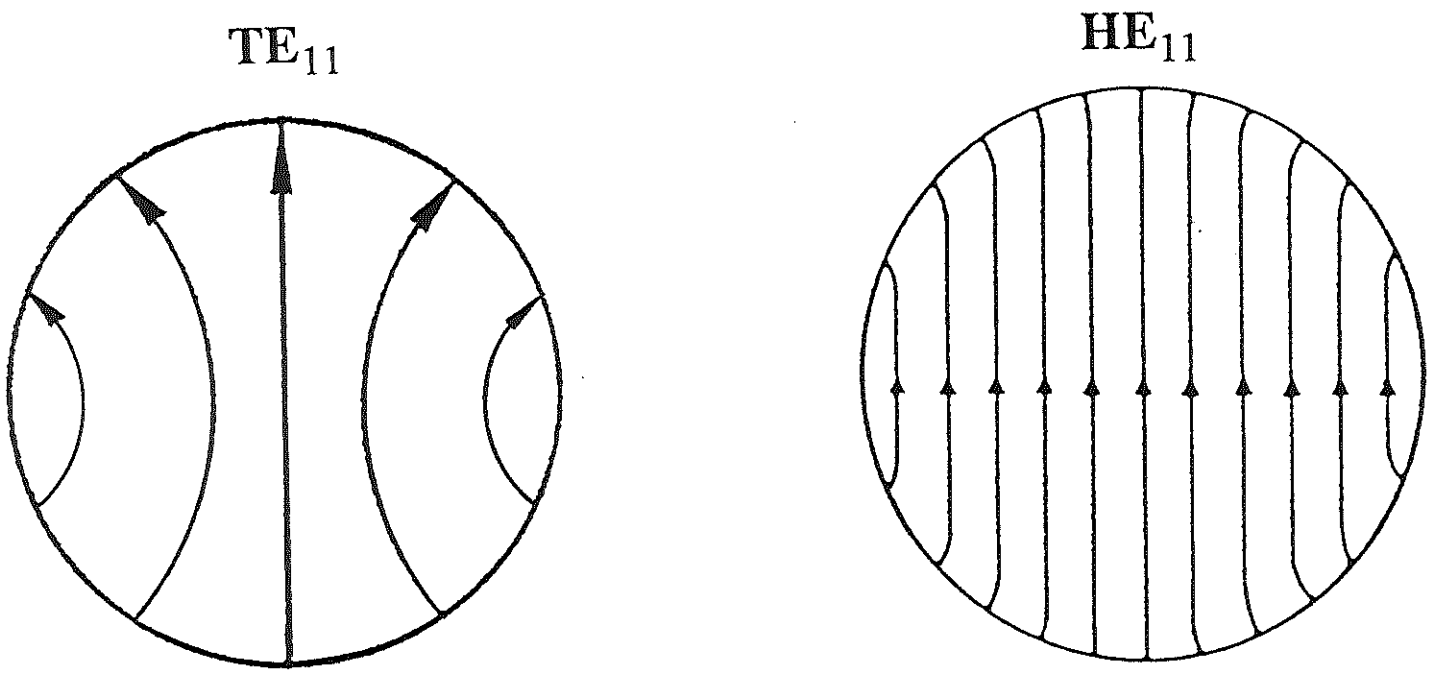

Figure 8. Circular Waveguide TE_{11} and Corrugated Waveguide HE_{11} Electric Field Distributions

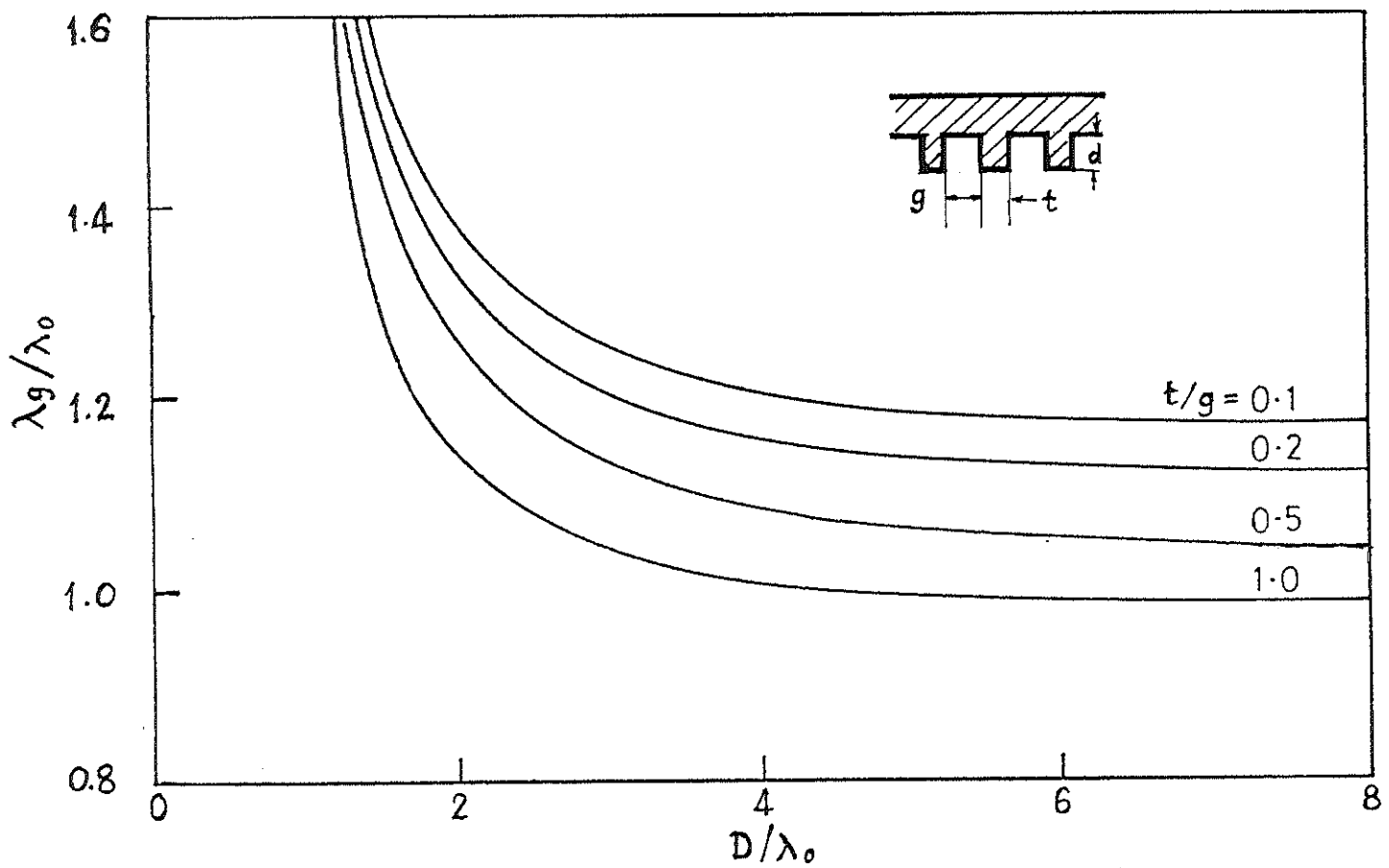

Figure 9. Space Harmonic Calculation for the Groove Depth Variations (D = 2a, g = 0.2 λ)

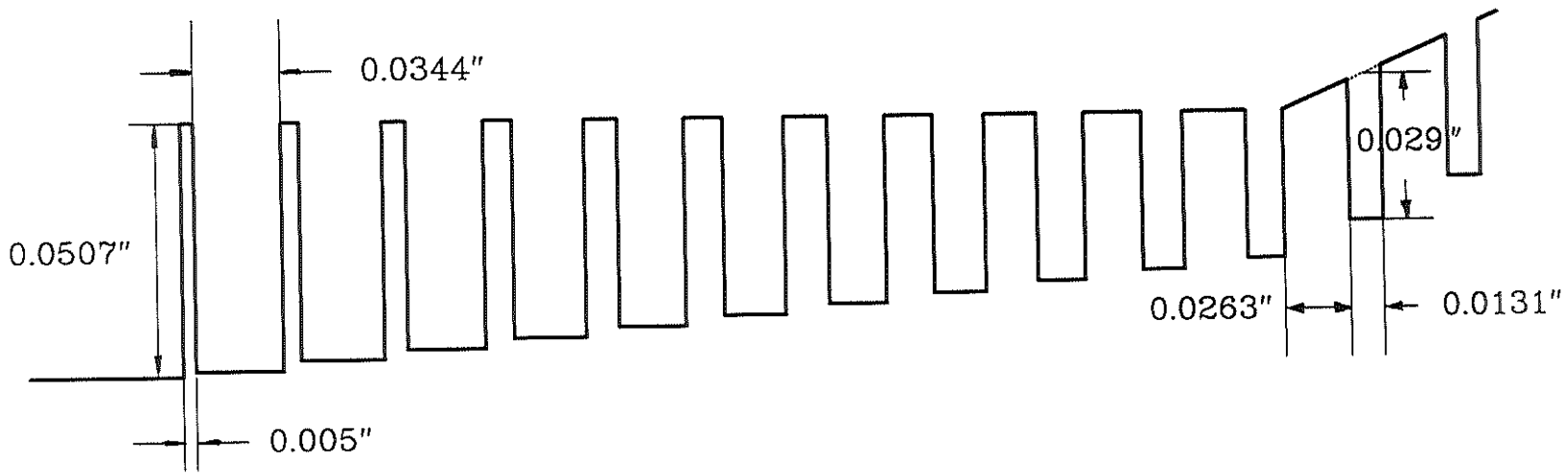

Figure 10. Throat Design for Wide Band Single-Mode Operation and Wide Band Impedance-Matching

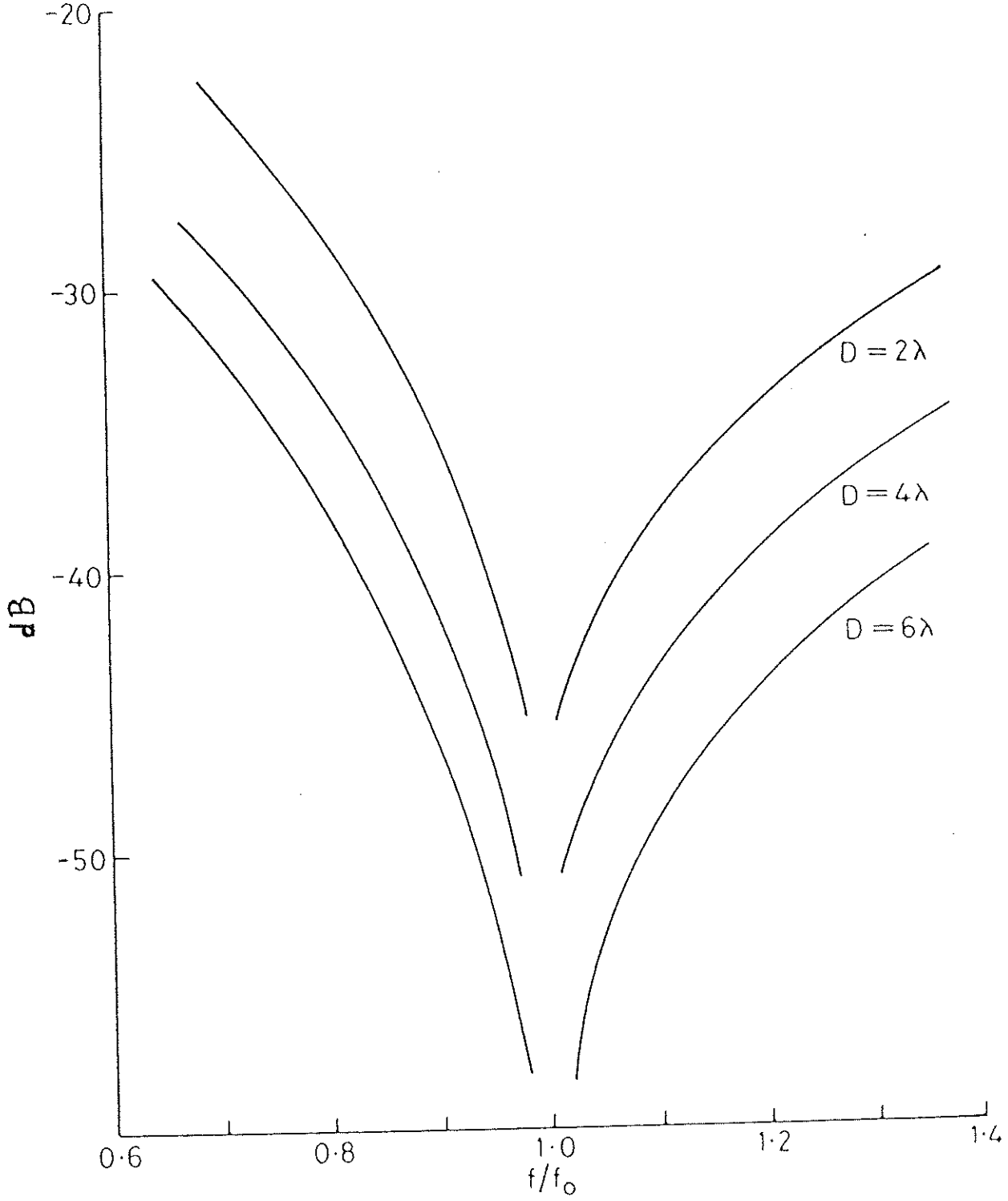

Figure 11. Bandwidth Characteristics of the Crosspolarization Levels

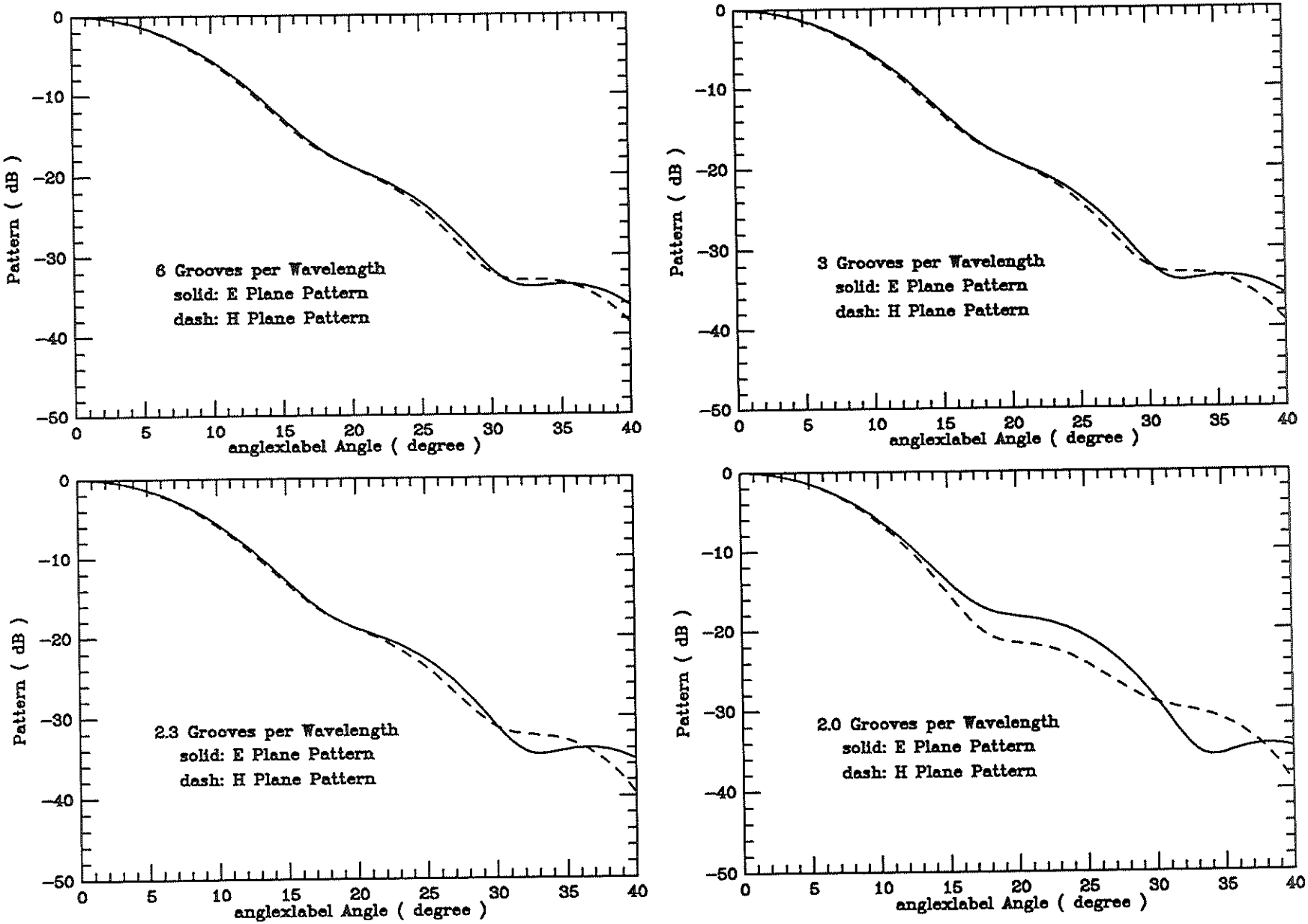

Figure 12. Groove Coarseness Tests

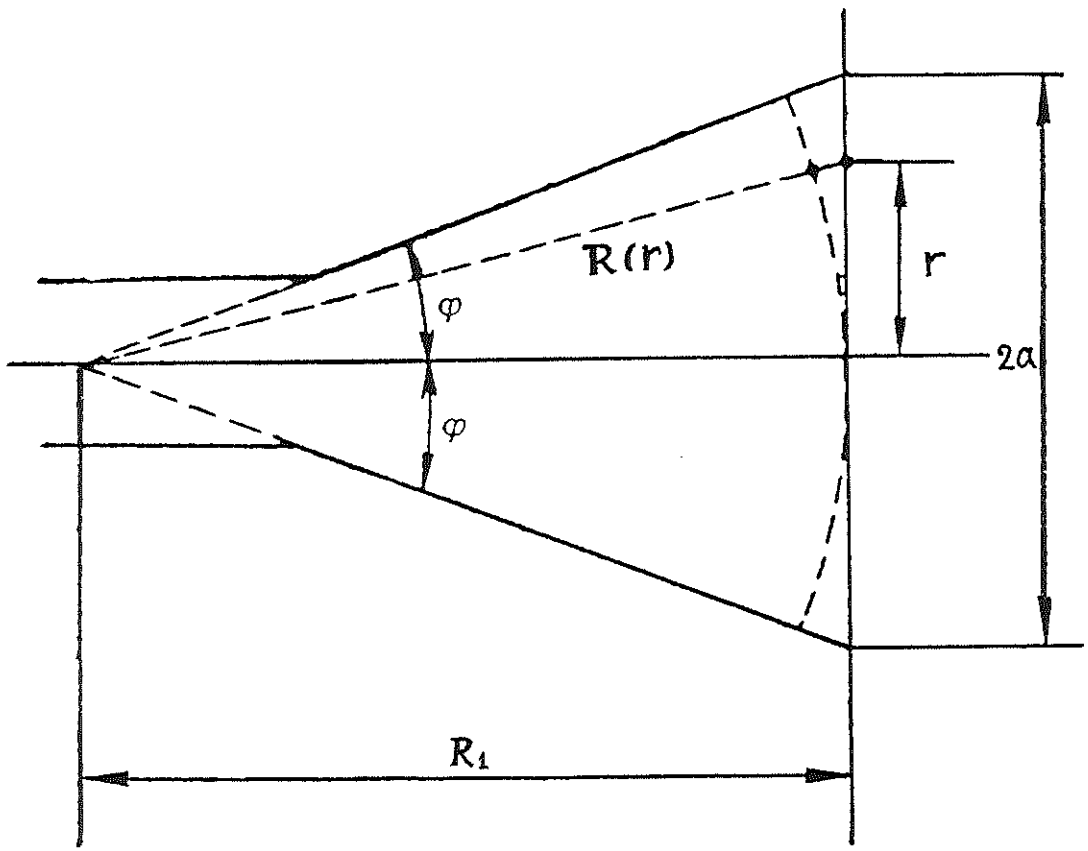

Figure 13. Aperture Phase Calculation for the Conical Corrugated Feed Horn

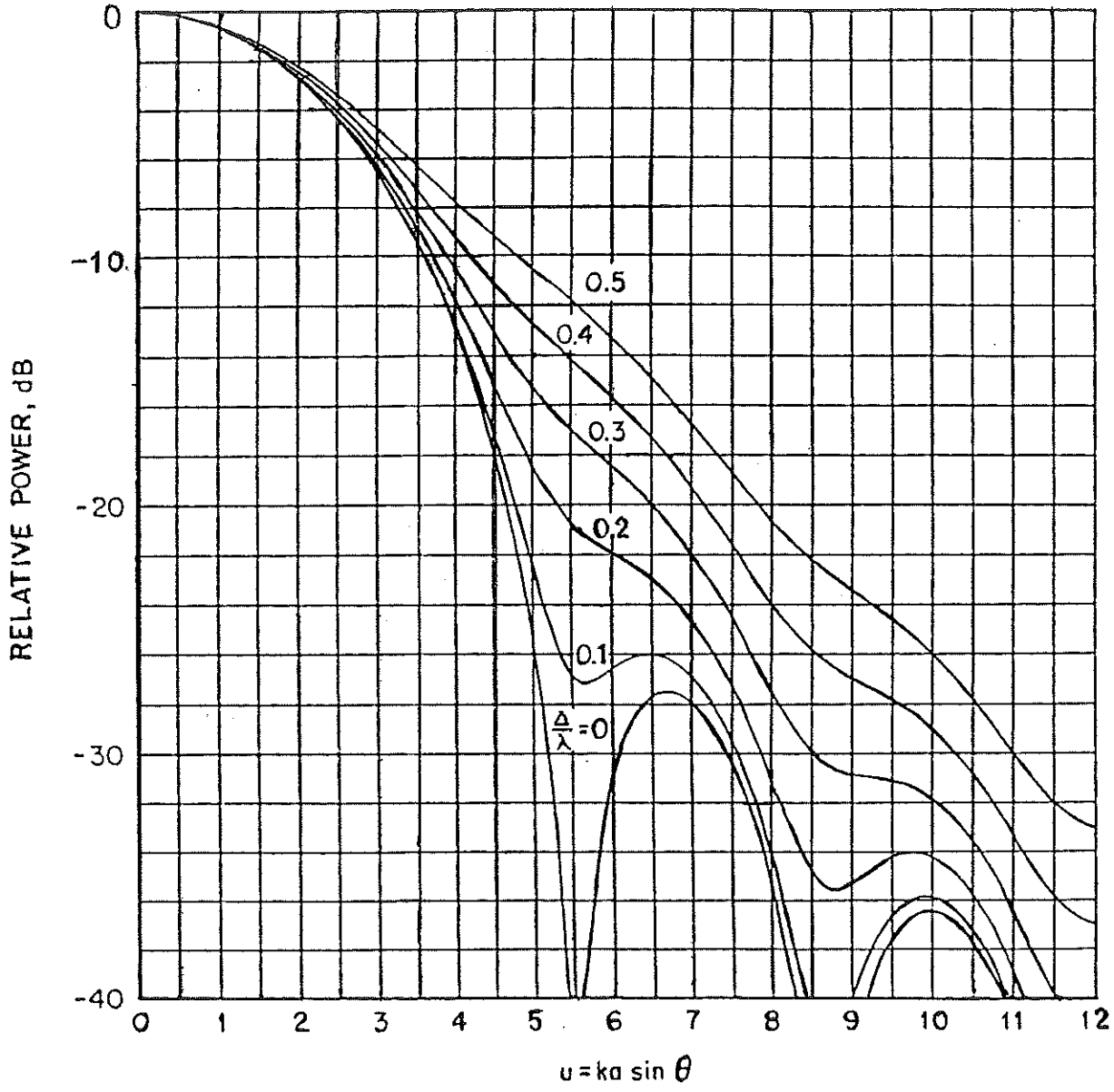

Figure 14. Universial Patterns for the Small-Flare-Angle Corrugated Horns Under Near-Balanced Conditions ($\Delta = a^2/2l$, where l is the flare length of the horn)

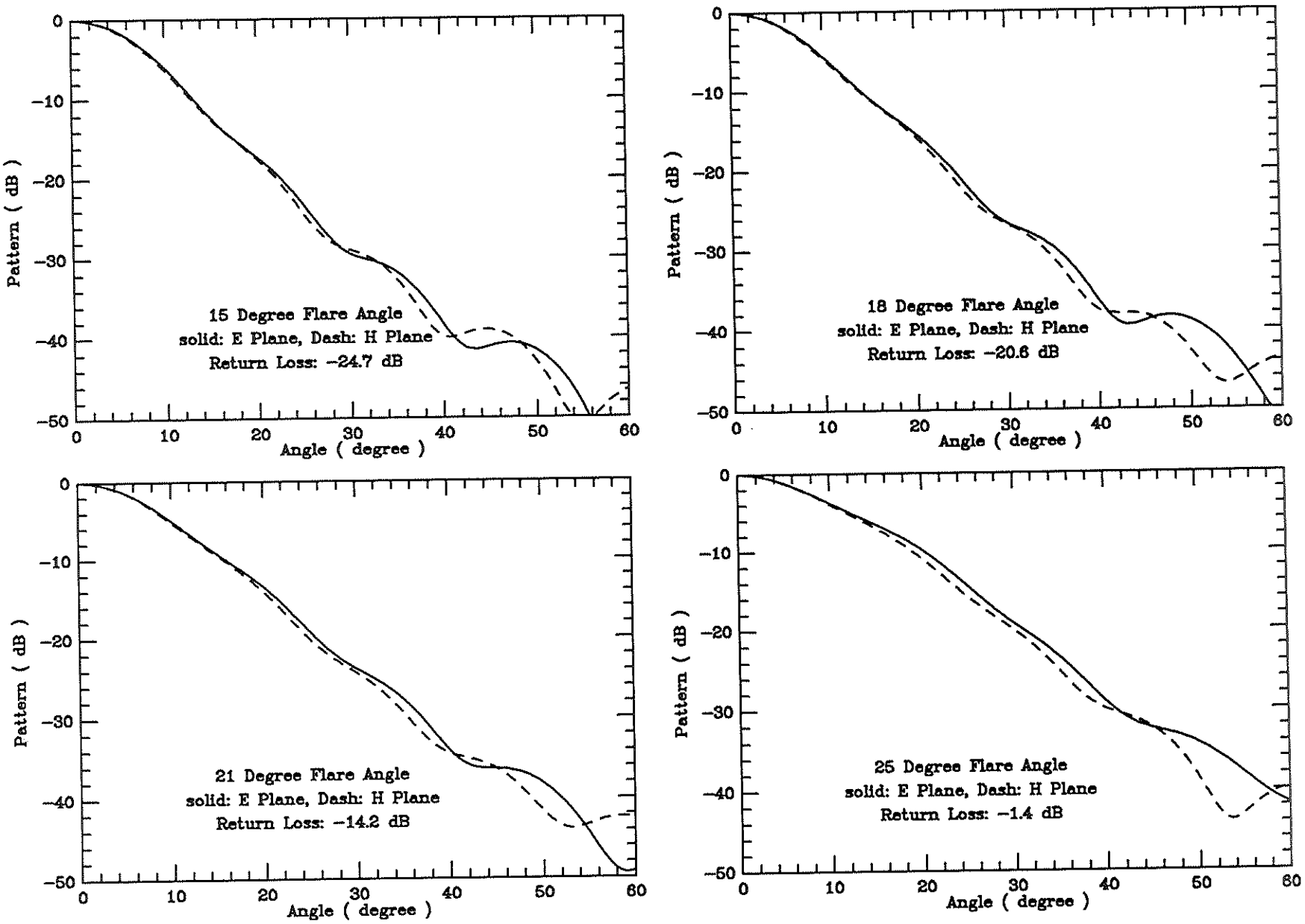

Figure 15. Flare Angle Tests

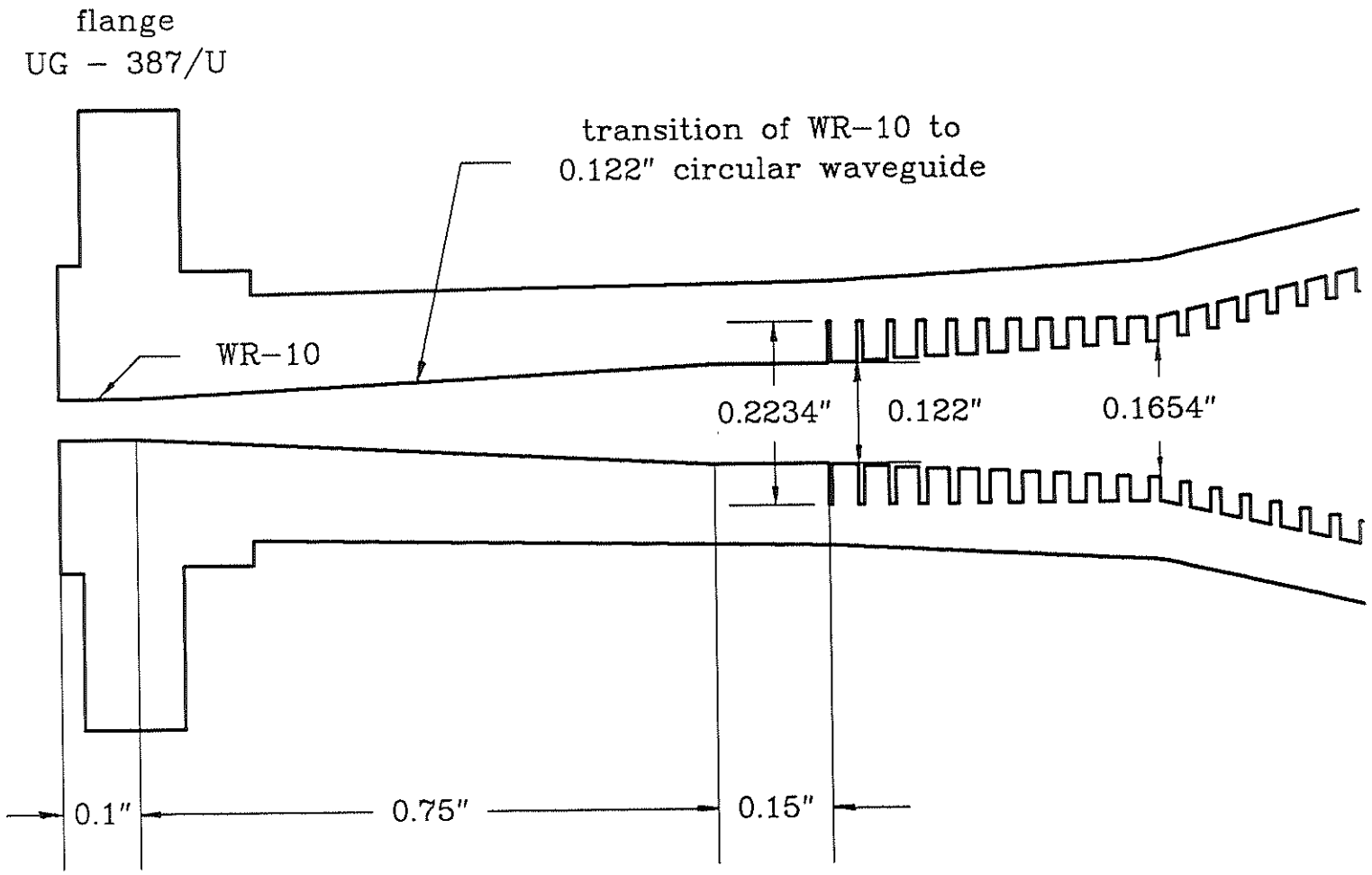

Figure 16. Waveguide Transition Section

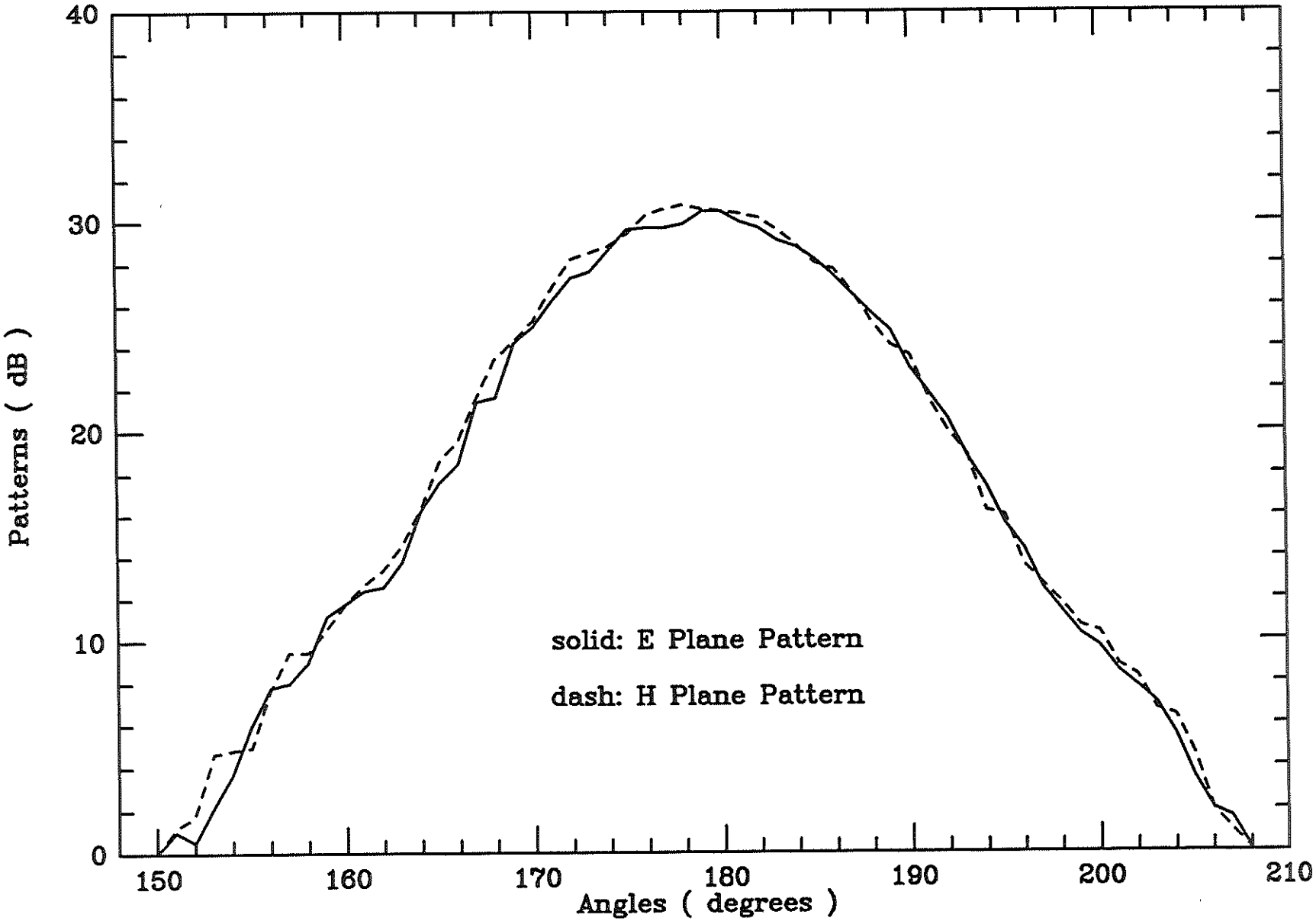

Figure 17. Measured Copolar Radition Patterns of the New Conical Horn

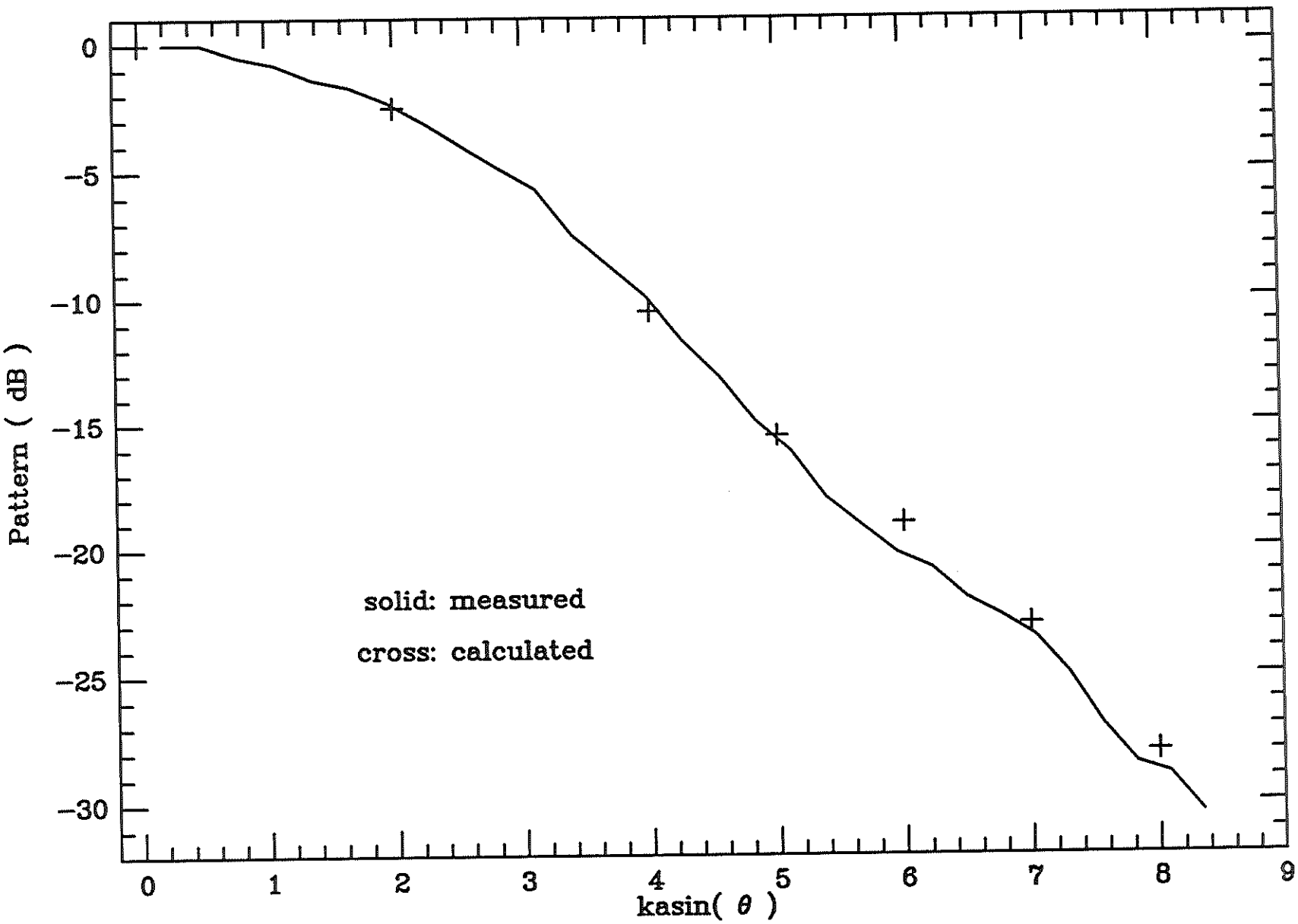

Figure 18. Comparison Between Theory and Measurement for the Copolar Radiation Patterns

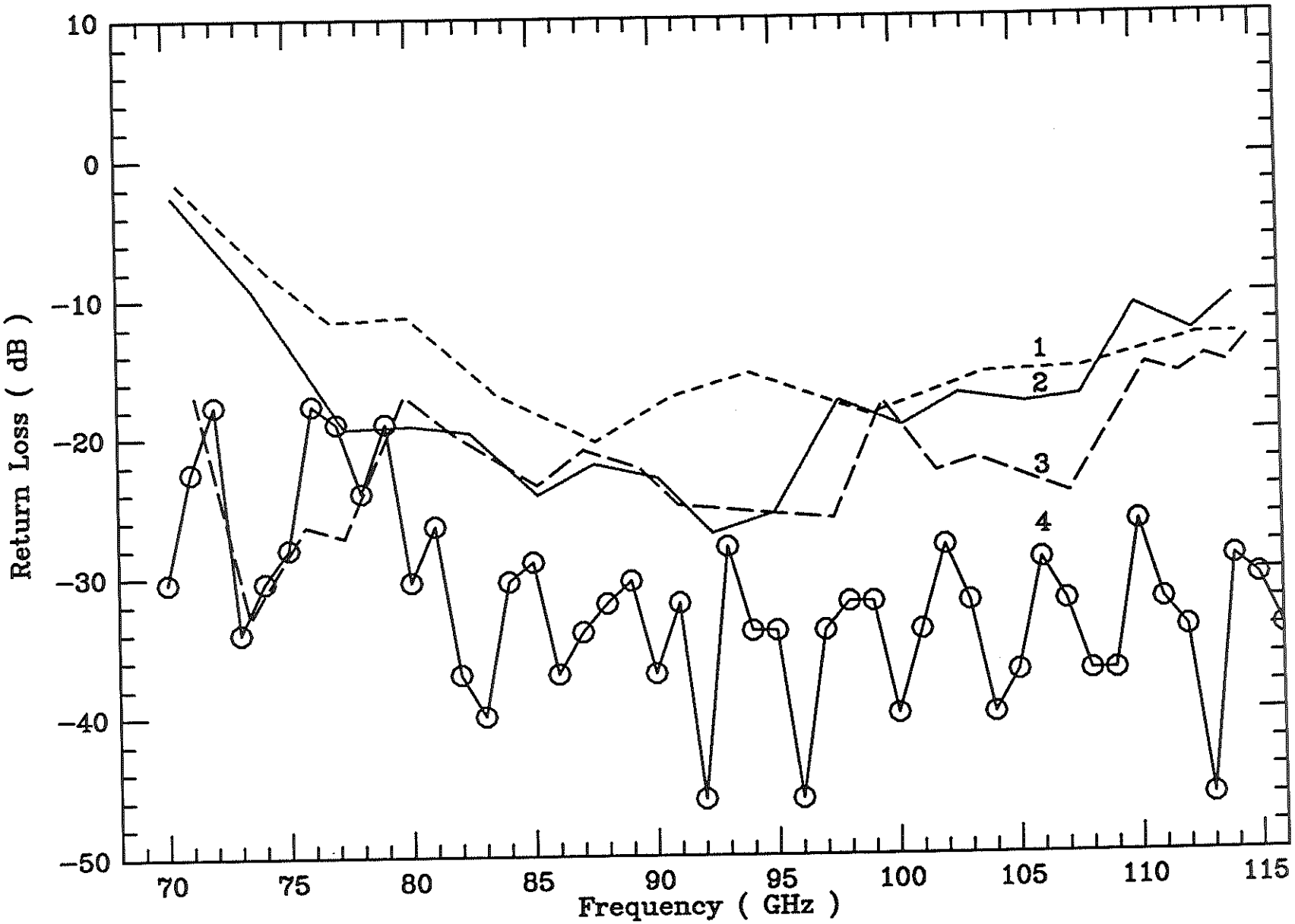

Figure 19. Comparison of the Return Losses of the 3 Old Hat Creek Horns (1,2,3) and the New Horn (4)

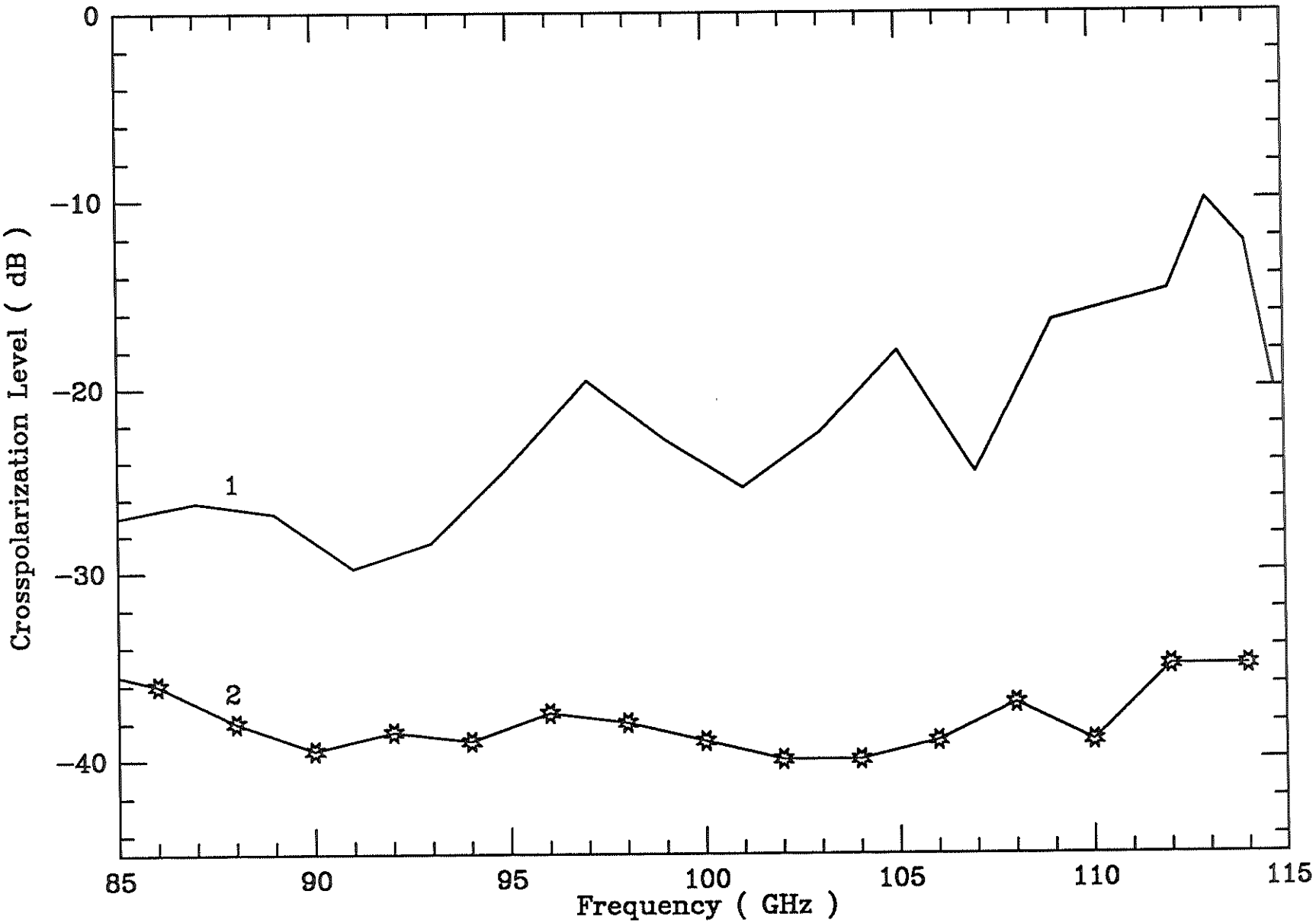

Figure 20. Comparison of the Crosspolarization Levels of the Old Horn (1) and the New Horn (2)

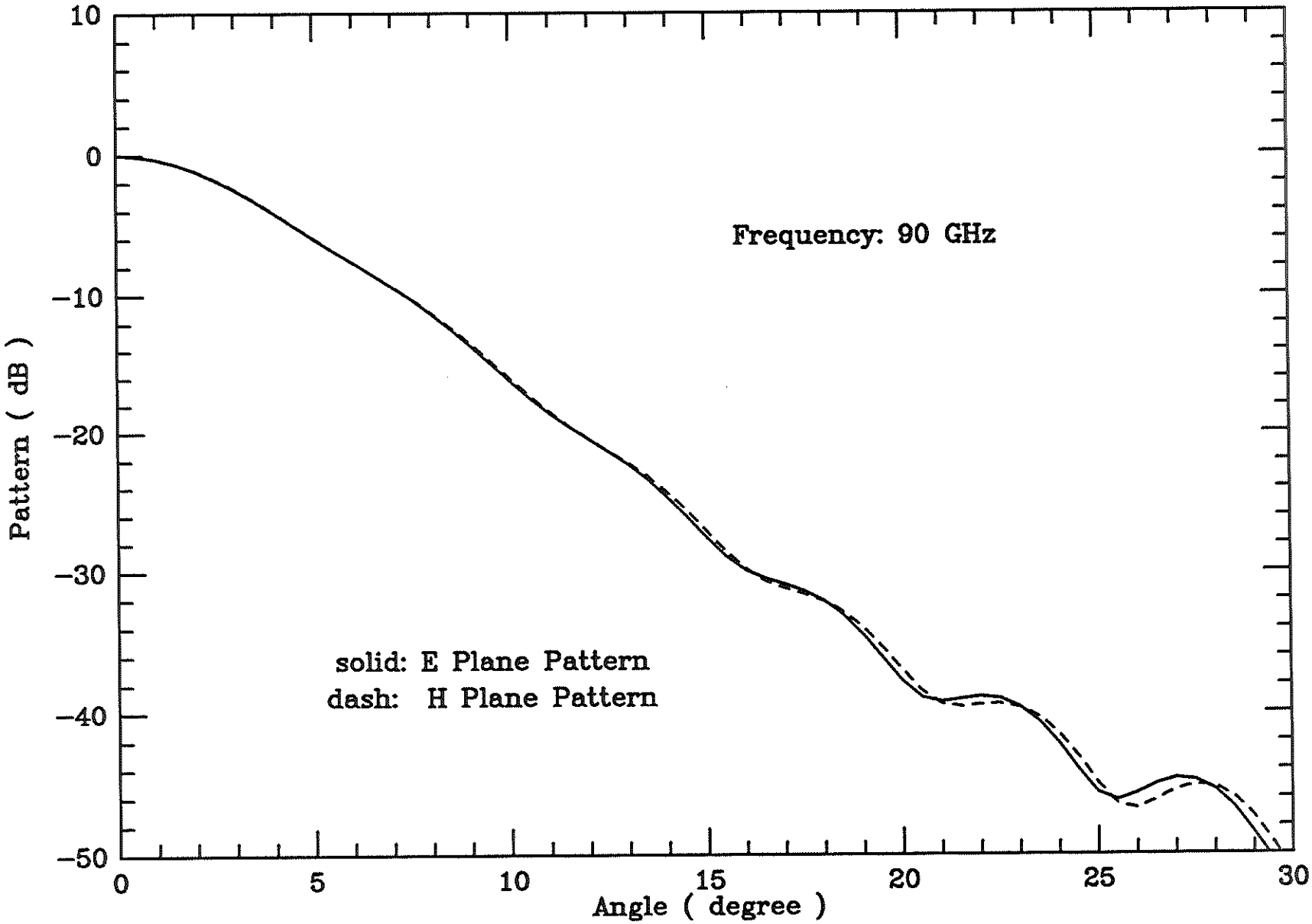

Figure 21. Calculated Amplitudes of the Old Horn at 90 GHz

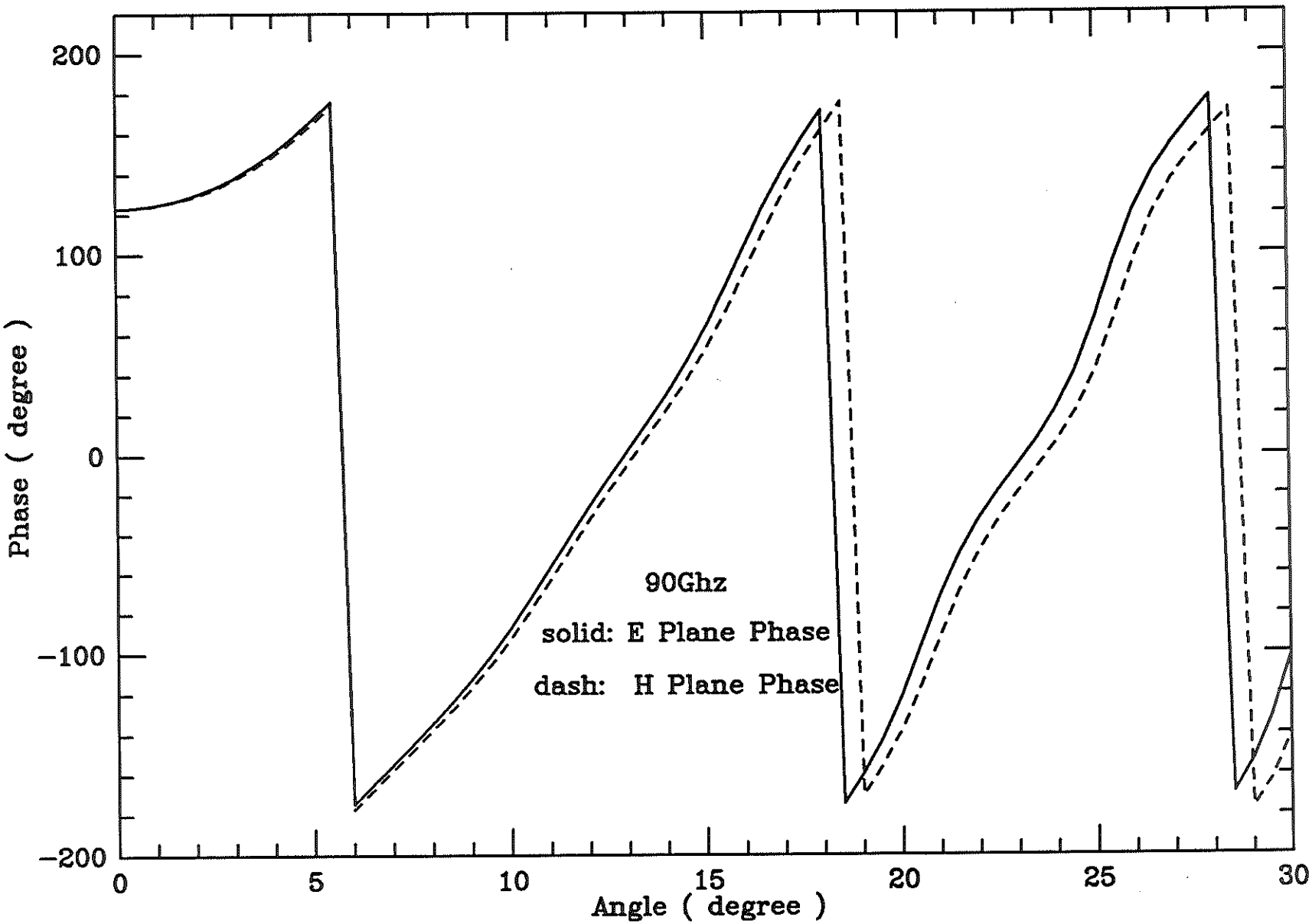

Figure 22. Calculated Phases of the Old Horn at 90 GHz

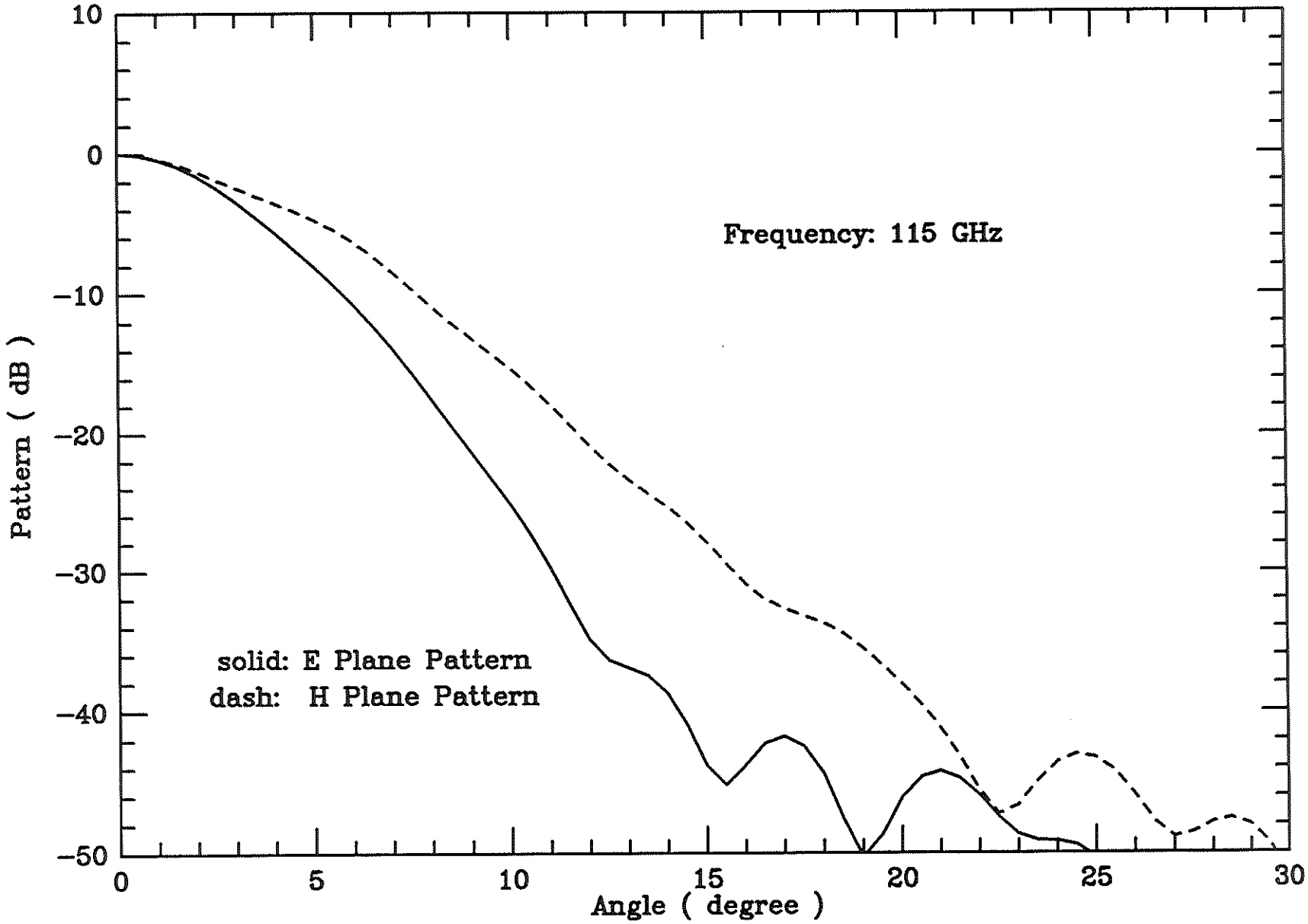

Figure 23. Calculated Amplitudes of the Old Horn at 115 GHz

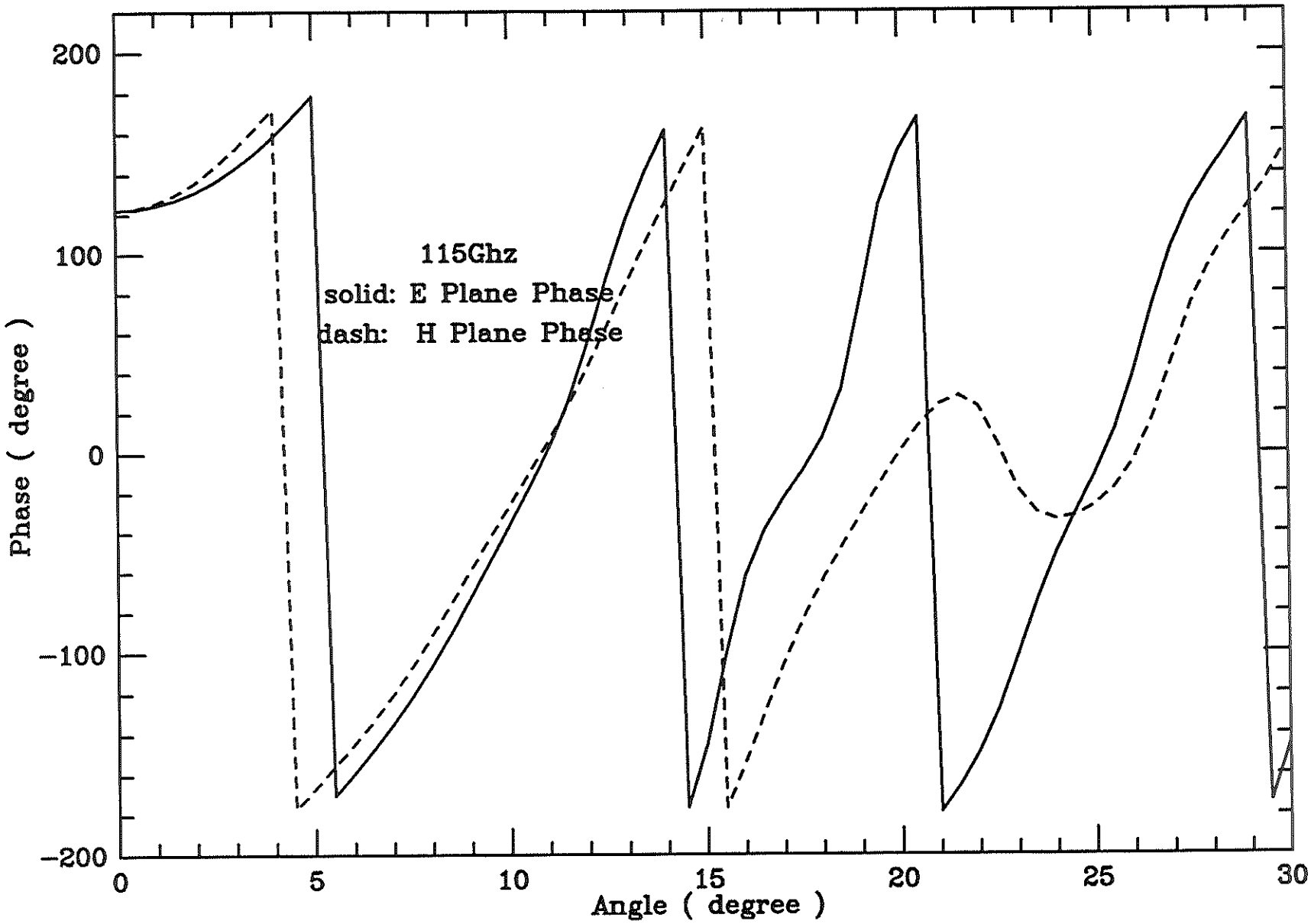

Figure 24. Calculated Phases of the Old Horn at 115 Ghz

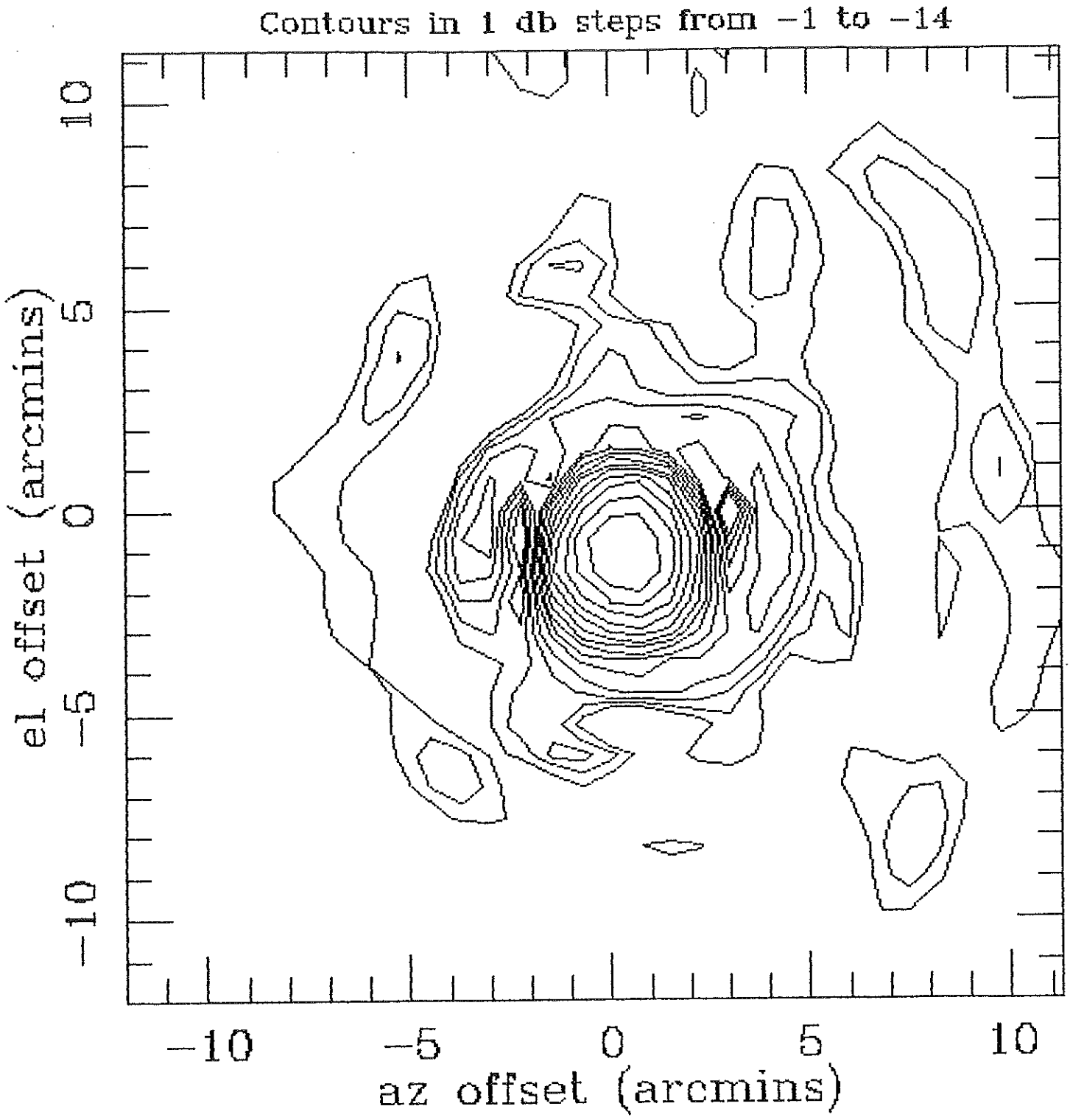

Figure 25. Holographical Measurements: Antenna 3 Beam Pattern on the Sky at 90 GHz

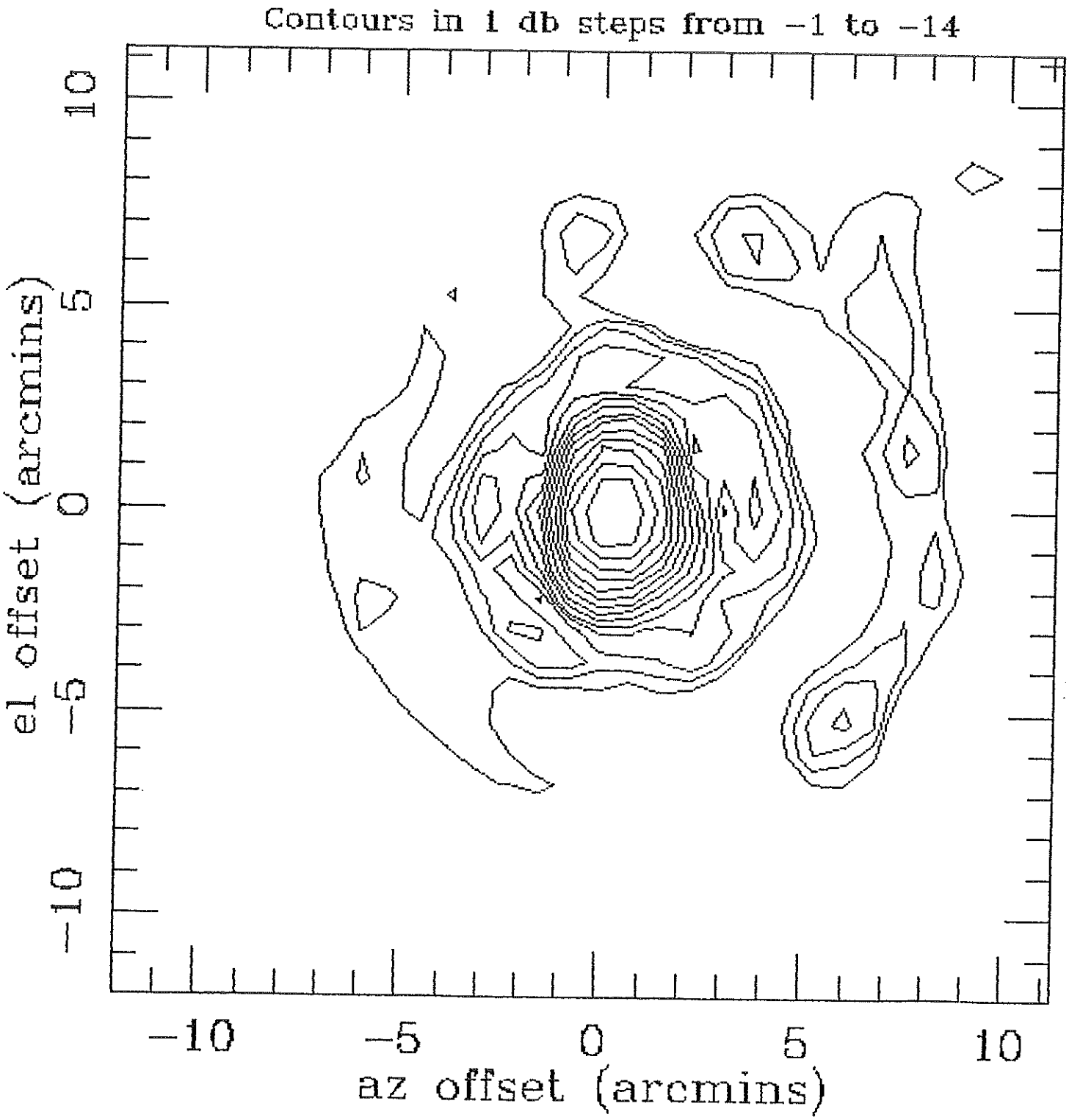

Figure 26. Holographical Measurements: Antenna 3 Beam Pattern on the Sky at 113 GHz

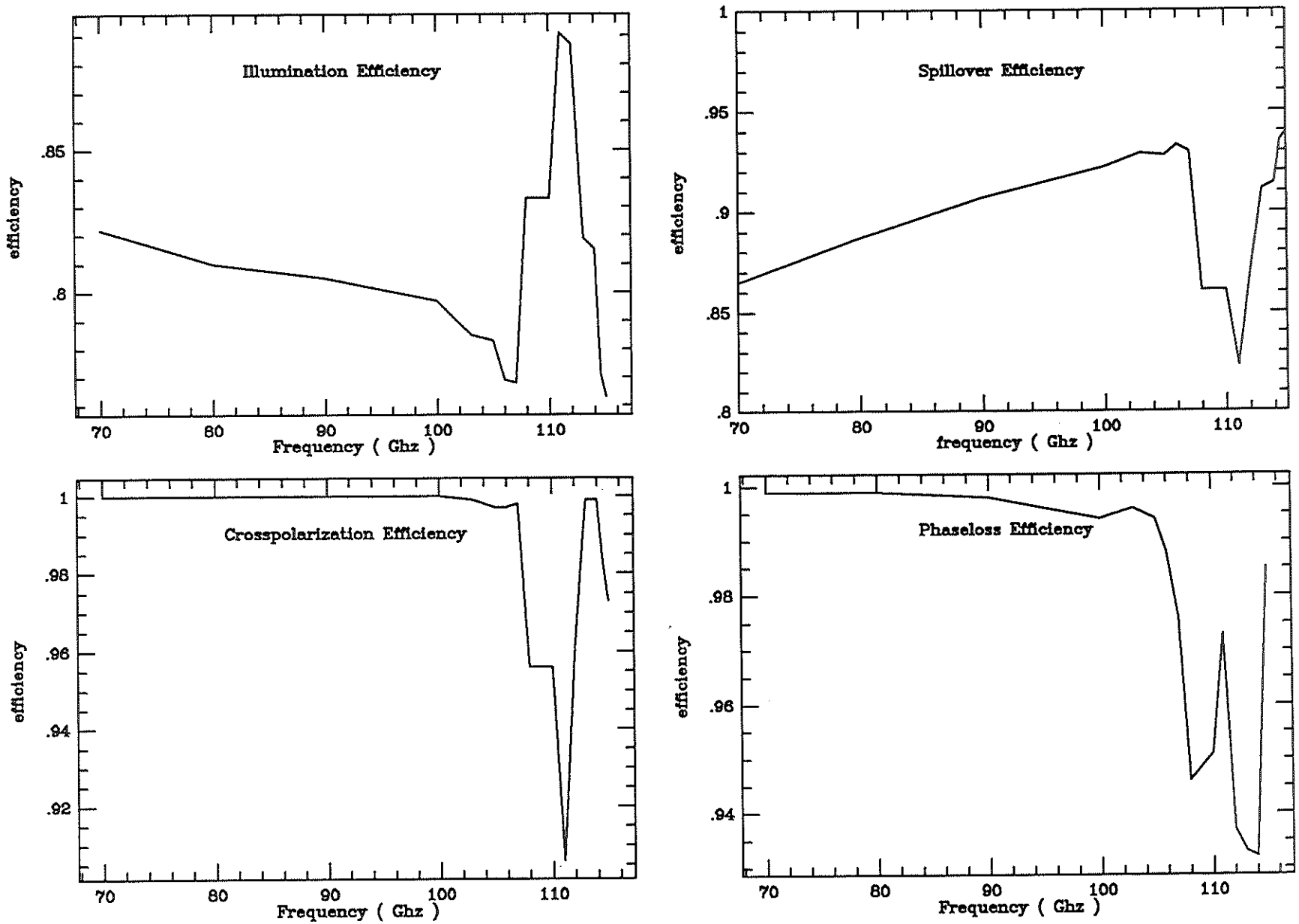

Figure 27. Calculated Contributions to Aperture Efficiencies Due to Crosspolaisation Loss, Phaseloss, Spillover Loss and Illumination Loss, for the Old Hat Creek Horn

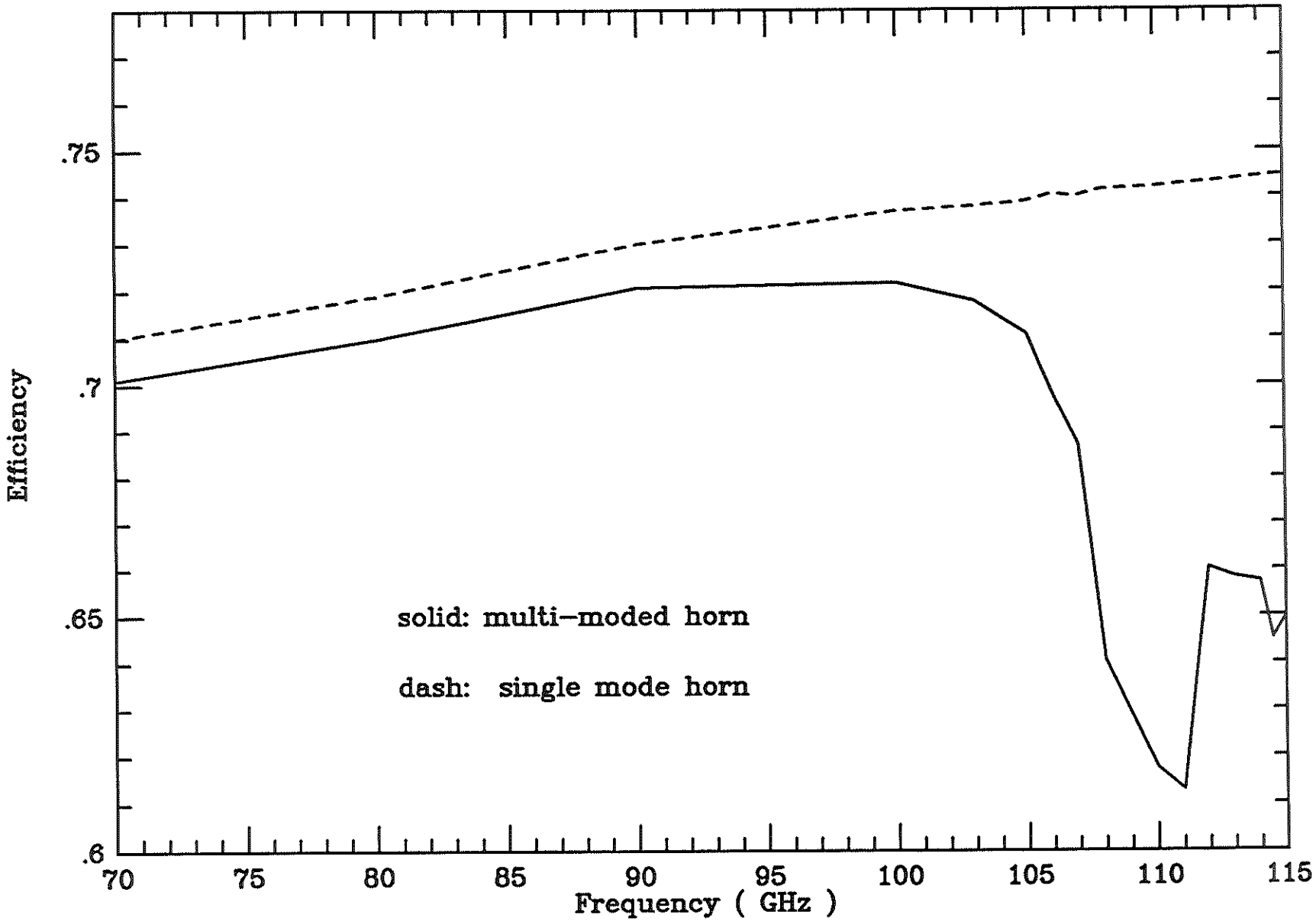

Figure 28. Comparison of the Calculated Total Efficiencies of the Old Hat Creek Horn and a Model Horn with the Same Outer Dimension But a Single-Moded Throat

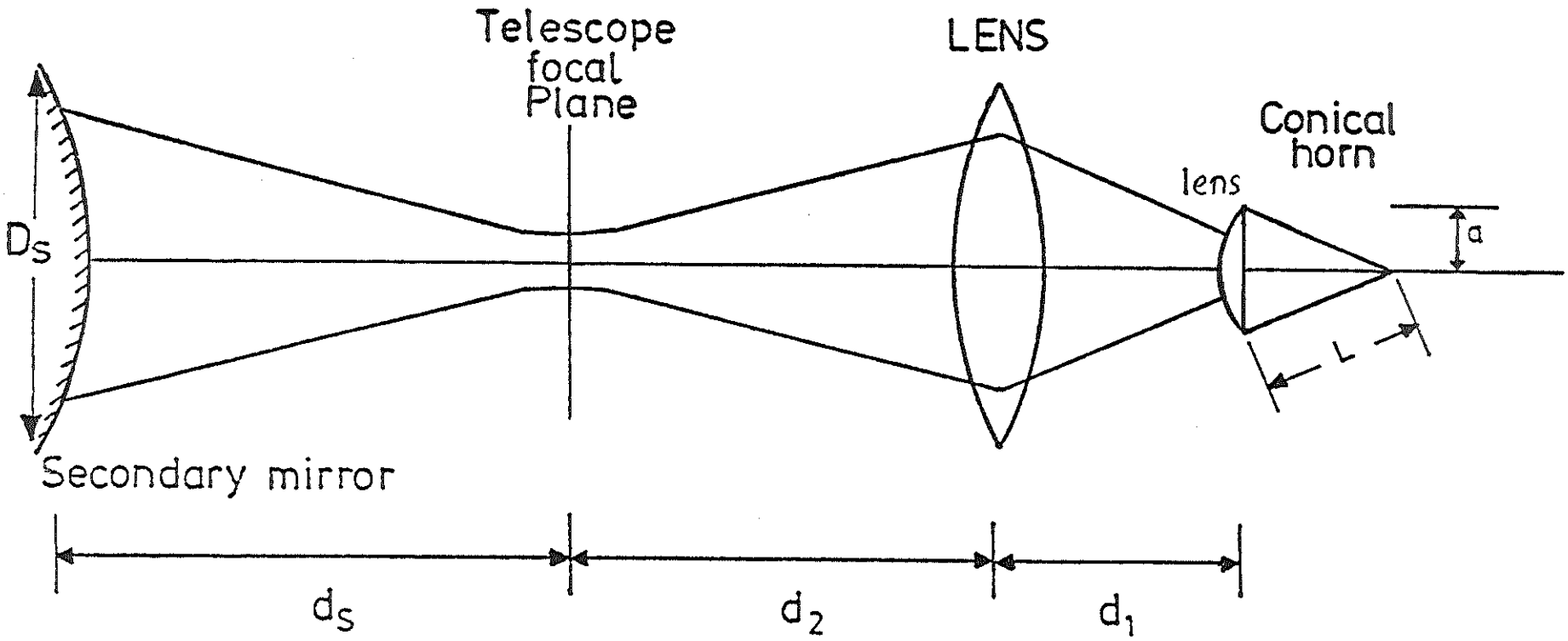

Figure 29. Tertiary Optics

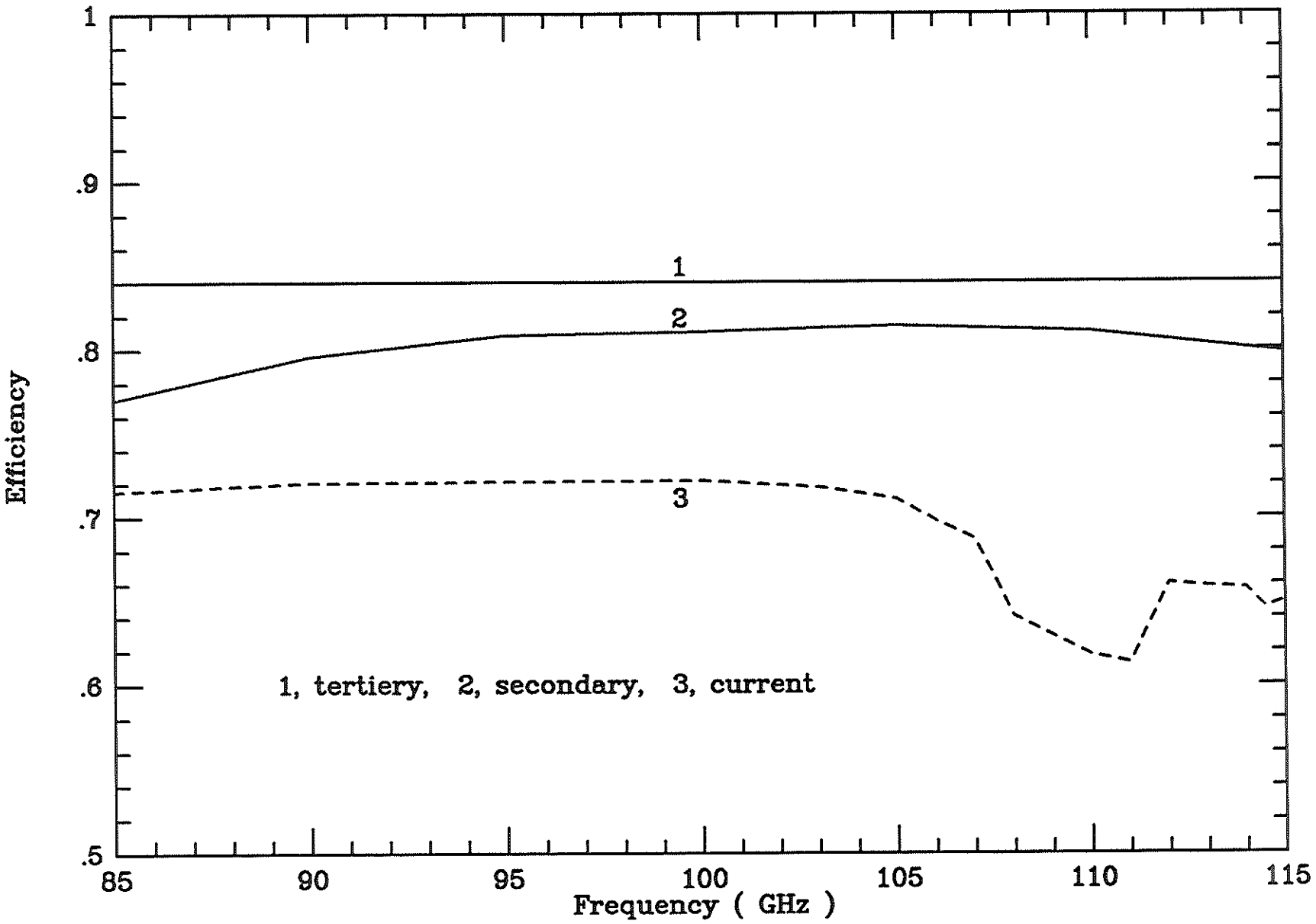

Figure 30. Calculated Aperture Efficiencies for Tertiary Optics, Secondary Optics and Current Horn

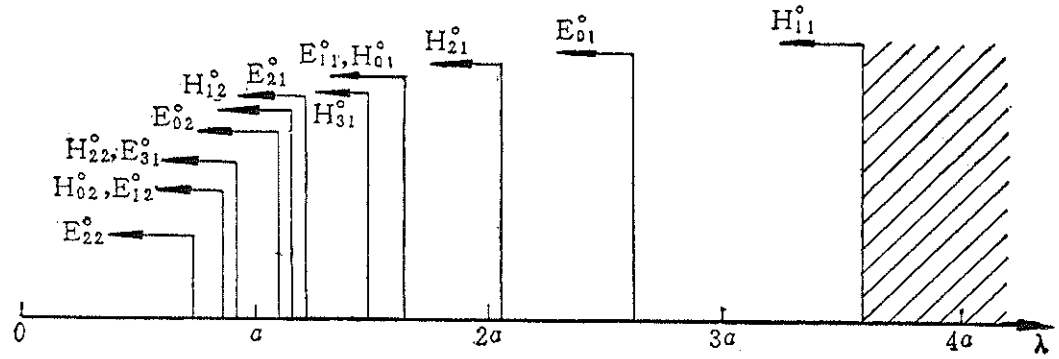

Figure 31. Circular Waveguide Modes and Their Cutoff Wavelengths ($H_{11} \equiv TE_{11}, E_{01} \equiv TM_{01}$, etc)